

Oden Institute REPORT 202107

April 2021

Removal of spurious outlier frequencies and modes from isogeometric discretizations of second- and fourth-order problems in one, two, and three dimensions

by

René R. Hiemstra, Thomas J. R. Hughes, Alessandro Reali, and Dominik Schillinger



Oden Institute for Computational Engineering and Sciences
The University of Texas at Austin
Austin, Texas 78712

Reference: René R. Hiemstra, Thomas J. R. Hughes, Alessandro Reali, and Dominik Schillinger, "Removal of spurious outlier frequencies and modes from isogeometric discretizations of second- and fourth-order problems in one, two, and three dimensions," Oden Institute REPORT 21-07, Oden Institute for Computational Engineering and Sciences, The University of Texas at Austin, April 2021.

Highlights

Removal of spurious outlier frequencies and modes from isogeometric discretizations of second- and fourth-order problems in one, two, and three dimensions

René R. Hiemstra, Thomas J. R. Hughes, Alessandro Reali, Dominik Schillinger

- We characterize outlier frequencies and modes for isogeometric discretizations of 1D, 2D, and 3D second- and fourth-order problems.
- We introduce a linear subspace of the original spline discretization that satisfies additional homogeneous boundary conditions of certain derivatives.
- The subspace of splines is outlier-free for homogeneous boundary conditions in second- and fourth-order problems, and maintains full accuracy.
- We verify that outlier removal increases the critical time-step size in explicit dynamics.

Removal of spurious outlier frequencies and modes from isogeometric discretizations of second- and fourth-order problems in one, two, and three dimensions

René R. Hiemstra^{a,*}, Thomas J. R. Hughes^b, Alessandro Reali^{c,d}, Dominik Schillinger^a

^a*Institute of Mechanics and Computational Mechanics, Leibniz University Hannover, Germany*

^b*Oden Institute for Computational Engineering and Sciences, The University of Texas at Austin, USA*

^c*Dipartimento di Ingegneria Civile e Architettura, Università di Pavia, Italy*

^d*Istituto di Matematica Applicata e Tecnologie Informatiche “Enrico Magenes”, Pavia, Italy*

Abstract

A key advantage of isogeometric discretizations is their accurate and well-behaved eigenfrequencies and eigenmodes. For degree two and higher, however, a few spurious modes appear that possess inaccurate frequencies, denoted as “outliers”. The outlier frequencies and corresponding modes are at the root of several efficiency and robustness issues in isogeometric analysis. One example is explicit dynamics where outlier frequencies unnecessarily reduce the critical time step. Another example is wave propagation where the inaccurate outlier modes may participate in the solution. In this paper, we first investigate the spurious outlier frequencies and corresponding modes of isogeometric discretizations of second- and fourth-order model problems and provide a complete characterization. We then devise a new approach that removes all outliers modes without negatively affecting the accuracy of the discretizations. Our approach is variationally consistent and works for a range of common boundary conditions on tensor product domains. We finally demonstrate that our approach allows a much larger critical time step, irrespective of polynomial degree, providing a pathway towards efficient higher-order explicit dynamics.

Keywords:

Isogeometric analysis, outlier frequencies, outlier modes, explicit dynamics, critical time-step

Contents

1	Introduction	4
2	Preliminaries	6
2.1	Natural frequencies and modes	6

*Corresponding author

Email addresses: rene.hiemstra@ibnm.uni-hannover.de (René R. Hiemstra),
hughes@ices.utexas.edu (Thomas J. R. Hughes), alereali@unipv.it (Alessandro Reali),
schillinger@ibnm.uni-hannover.de (Dominik Schillinger)

2.2	Discrete natural frequencies and modes	6
2.3	Measures of error	7
3	Second- and fourth-order eigenvalue problems	7
3.1	Free axial vibration of a bar	7
3.2	Free transverse vibration of a thin Bernoulli-Euler beam	8
3.3	Multidimensional problems	9
3.4	Simplifications on tensor product domains	10
4	Characterization of outlier frequencies and modes	11
4.1	A one-dimensional example	11
4.2	Outlier modes and frequencies of univariate discretizations	11
4.3	Outlier modes and frequencies of multivariate tensor product discretizations	13
5	Outlier-free extraction operator	15
5.1	Univariate B-splines	15
5.2	Outlier-free linear subspace \mathbb{S}^-	16
5.3	A basis for \mathbb{S}^-	17
5.4	Tensor product spaces	19
5.5	Mapped geometry	19
6	One-dimensional study of spectra and modes	21
6.1	Presentation of the data	22
6.2	Second-order eigenvalue problems: free axial vibration of a bar	22
6.3	Fourth-order eigenvalue problems: free transverse vibration of a beam	25
7	Multivariate study of spectra and modes	28
7.1	Presentation of the data	28
7.2	Second-order eigenvalue problems	29
7.3	Fourth-order eigenvalue problems	38
8	Application in explicit dynamics	44
8.1	Explicit dynamics of an annular membrane	44
8.2	Study of the critical time-step	46
9	Conclusion	50
Appendix A	Outlier-free extraction algorithm	51
Appendix B	Compatibility with boundary forces and moments	51
Appendix C	Asymptotic approximation of beam modes	53

Appendix D	Computation of multivariate spectra	53
Appendix D.1	Correct identification of analytical and numerical eigenmodes	53
Appendix D.2	Error analysis of multivariate spectra	55

1. Introduction

Isogeometric analysis (IGA) was introduced in 2005 with the primary goal to improve the design-through-analysis process [1]. A somewhat fortuitous result was that much better accuracy and robustness was typically achieved, on a per-degree-of-freedom basis, compared with classical C^0 finite element analysis (FEA) [2, 3, 4, 5]. From a theoretical viewpoint, this can be attributed to the much better spectral properties of IGA compared with FEA [6, 7, 8, 9]. In FEA, higher-order p elements produce so-called *optical branches*¹ of frequency spectra, which cause deteriorating accuracy of the higher modes and have been identified as contributors to spurious high modal response in dynamics [11], where modal errors propagate and may persist for all time. Algorithmic damping of time discretization methods may not be sufficient to restore quantitative accuracy [7]. A similar issue can be expected in non-linear problems, where, due to modal coupling, all modes may take part in the numerics, and modal errors are transferred to low modes and vitiate the numerical solution.

It has been known for some time that the upper part of the FEA spectrum is inaccurate [11, 12], but a more recent observation is that the errors diverge with polynomial degree p [6, 7, 8, 9]. These studies also showed that for smooth isogeometric function spaces, almost the entire spectrum converges with increased polynomial order. Furthermore, almost all the modes are indistinguishable from the L^2 best approximation of the corresponding analytical modes [7]. This creates intriguing possibilities for IGA in structural dynamics, specifically, higher-order spatial accuracy concomitant with increased robustness. One stumbling block that still persists, however, was reported in [13, 14]: a relatively small portion of the modes form an optical branch, the so-called “outliers”. The corresponding modes are ill-behaved and may affect robustness. The corresponding frequency values are much larger than the exact values, thus posing an efficiency problem as they may reduce stable critical time-steps in explicit dynamics.

In the first paper on isogeometric structural vibrations [14], the outlier frequencies were eliminated by employing a non-linear parameterization of the domain, obtained through a uniform distribution of the control points. It was observed, empirically, that this choice eliminates outliers for any p , but a sound mathematical explanation has not been delivered. The approach has not gained traction in mathematics and engineering circles. The prime reason is that such a non-linear parameterization of the domain is generally not possible without introducing geometric approximations in the CAD geometry. This is in conflict with one of the fundamental principles of isogeometric analysis, namely to employ the same geometry description for both design and analysis. Another reason is that the first p elements near the boundary quickly grow in size², thus leading to a loss of spatial accuracy of the low modes and frequencies. This observation has so far not been published in the literature, but has been verified by the authors of this work. Other unpublished results, verified by us, that seem to mitigate or remove outlier frequencies are: (1) to keep the size of the boundary elements twice as large as the interior elements in combination with a linear parameterization of the domain; or (2) lower the polynomial degree to linear functions near the

¹as described in [10]

²The knots may be distributed in a non-uniform manner such that their image under the non-linear parameterization is uniform. There is, however, no closed form solution for this placement of the knots. Furthermore, it has been verified that this choice also leads to a loss of spatial accuracy in the low modes and frequencies.

boundary using multi-degree spline techniques [15, 16]. Both approaches may mitigate or remove outliers, but, unsurprisingly, have been found to negatively impact accuracy in the remainder of the spectrum.

The first contribution of this paper is to provide a better understanding of the outlier modes and frequencies. To this end, we provide a complete characterization of outlier modes and frequencies arising in isogeometric analysis of structural vibrations involving second- and fourth-order differential operators. In particular, we determine the number of outliers for all common sets of homogeneous boundary conditions in univariate problems, and then generalize these observations to the multidimensional setting. The second contribution of this paper is the introduction of a procedure to systematically remove the outliers, without affecting accuracy in the remainder of the spectrum and modes. The methodology can be used with any discretization method (Galerkin, collocation, etc.) and any mass matrix (consistent, lumped, etc.), and is investigated herein for the Galerkin method with consistent mass matrix. The fundamental idea that underlies our approach is the notion that analytical solutions to eigenvalue problems satisfy a sequence of eigenvalue problems, involving higher-order self-adjoint operators, with additional homogeneous boundary constraints. Once these constraints are built into the trial space, the outlier modes disappear. The approach is variationally consistent because the additional constraints are satisfied by the analytical solution. An interesting alternative is to impose these boundary conditions weakly by means of a penalty term or a Nitsche formulation. We are aware of a recent, independent study in this direction [17]. However, an advantage of imposing the conditions strongly is that the outlier modes are removed entirely. This is not the case with a weak approach, which may only stabilize the frequencies, not the modes. The constraints are conveniently encoded in a Bézier extraction operator, which makes our approach both efficient and simple to implement. We test our method for second- and fourth-order problems by investigating the spectral properties of smooth splines with and without outlier removal in the one-dimensional and multidimensional setting. In the multidimensional cases, we utilize new orderings of the frequency and mode shape errors that provide better representations. The improved accuracy obtained with our method for frequencies and mode shapes is considerable, particularly in the multivariate setting. We verify that these gains in spatial accuracy are maintained when applying the approach in explicit dynamics of an annular membrane. Finally, we perform numerical tests to confirm that a larger critical time-step size can be maintained when the outliers are removed, with little additional complexity and without additional cost.

The paper is structured as follows: In Section 2, we briefly review some of well-known topics in structural vibrations and modal analysis, and discuss error norms that will be used in the paper. In Section 3, we discuss the eigenvalue problems that are considered as test cases, present their classical solutions, and describe the essential notion from an analytical perspective that later will motivate the proposed outlier removal technique. Section 4 provides a complete characterization of outlier modes and frequencies in the context of univariate and multivariate second- and fourth-order problems. In Section 5, we derive a subspace of the original spline space that is outlier-free by construction. We present a basis for this space, encoded in an extraction operator. In Sections 6 and 7, we investigate the spectral approximation properties of the subspace in the one- and multi-dimensional setting. In Section 8, we demonstrate that outlier-free discretizations allow a significantly larger critical time-step size in two-dimensional explicit dynamics. Finally, in Section 9, we draw conclusions and make recommendations for future research.

2. Preliminaries

We briefly discuss the equation of motion of the free unforced structural vibration problem and recall modal decomposition in the infinite-dimensional as well as the discrete setting. We then discuss useful norms for evaluation of the error made across the full range of modes.

2.1. Natural frequencies and modes

The undamped, unforced equations of motion, governing free vibration of a linear (∞ -dimensional) structural system, are

$$\mathcal{M} \frac{d^2 u}{dt^2}(\mathbf{x}, t) + \mathcal{K} u(\mathbf{x}, t) = 0, \quad \mathbf{x} \in \Omega, \quad t > 0 \quad (1)$$

Here, \mathcal{M} and \mathcal{K} are the mass and stiffness operators, respectively, which are linear and self-adjoint. Furthermore, $u(\mathbf{x}, t)$ is the displacement, and $d^2 u/dt^2$ denotes the acceleration.

The generalized eigenvalue problem

$$(\mathcal{K} - \omega_n^2 \mathcal{M}) U_n(\mathbf{x}) = 0 \quad (2)$$

yields a set of linearly independent spatial modes $U_n(\mathbf{x})$ that form a basis in space. The displacement can then be expanded as $u(\mathbf{x}, t) = \sum_n U_n(\mathbf{x}) \cdot T_n(t)$, using separation of variables. The time-dependent coefficients $T_n(t)$ satisfy the equation

$$\frac{d^2 T_n(t)}{dt^2} + \omega_n^2 T(t) = 0. \quad (3)$$

The solution is of the form $T_n(t) = C_+ \exp(i\omega_n t) + C_- \exp(-i\omega_n t)$ and describes an oscillation at a frequency ω_n , where C_+ and C_- are constants to be determined from boundary conditions.

2.2. Discrete natural frequencies and modes

Spatial discretization of the equation of motion in (1) leads to the semi-discrete system of equations

$$\mathbf{M} \frac{d^2 \mathbf{u}^h}{dt^2} + \mathbf{K} \mathbf{u}^h = \mathbf{0} \quad (4)$$

where \mathbf{M} and \mathbf{K} denote the consistent mass and stiffness matrix, respectively, $\mathbf{u}^h = \mathbf{u}^h(t)$ is the displacement vector, and $d^2 \mathbf{u}^h/dt^2$ is the acceleration vector. Analogous to the continuous case, the discretized eigenvalue problem

$$(\mathbf{K} - (\omega_n^h)^2 \mathbf{M}) \mathbf{U}_n^h = \mathbf{0} \quad (5)$$

leads to a linearly independent set of discrete modes, \mathbf{U}_n^h , $1, 2, \dots, N$, that provide a basis for the spatial component of displacement.

Using separation of variables, the discrete solution may be represented as $\mathbf{u}^h(t) = \sum_n \mathbf{U}_n^h \cdot T_n^h(t)$. Analogous to the continuous case, the time-dependent component is given by $T_n^h(t) = C_+ \exp(i\omega_n^h t) + C_- \exp(-i\omega_n^h t)$, which describes an oscillation at a frequency ω_n^h .

2.3. Measures of error

In Sections 6 and 7, we will investigate, by numerical experiments, the errors made, globally, across the whole range of frequencies and modes. We will use the following measures of error:

$$\frac{|\omega_n - \omega_n^h|}{\omega_n} \quad (\text{Normalized frequency error}) \quad (6a)$$

$$\frac{\|U_n - U_n^h\|_{L^2}}{\|U_n\|_{L^2}} \quad (\text{Normalized } L^2 \text{ mode error}) \quad (6b)$$

Importantly, measures of frequency error and L^2 modal errors can be combined to evaluate the mode error in the energy norm. Provided that $\|U_n\|_{L^2} = \|U_n^h\|_{L^2}$, the following relation holds for every mode [12, Chapter 6, Section 3, Page 233]:

$$\frac{\|U_n - U_n^h\|_E^2}{\|U_n\|_E^2} = \frac{\|U_n - U_n^h\|_{L^2}^2}{\|U_n\|_{L^2}^2} + \frac{\omega_n^2 - (\omega_n^h)^2}{\omega_n^2} \quad \forall n = 1, 2, \dots, N. \quad (7)$$

This relationship, denoted as the *Pythagorean eigenvalue error theorem*, is used extensively in [7] to evaluate both finite element and spline approximations of eigenvalue, boundary-value, and initial-value problems. We refer to [7] for an in-depth discussion of error measures used in eigenvalue problems.

3. Second- and fourth-order eigenvalue problems

This section contains a summary of the univariate and multivariate second- and fourth-order eigenvalue problems studied in this paper. The focus is on free vibration of rods and beams with several sets of common boundary conditions. In particular, we discuss that the normal modes satisfy a sequence of higher-order eigenvalue problems, which is used to determine additional boundary constraints involving certain higher-order derivatives.

3.1. Free axial vibration of a bar

We consider free vibration of a uniform elastic bar of unit length with unit material parameters. The normal mode U_n satisfies the eigenvalue problem: find $(U_n, \omega_n) \in \mathcal{U} \times \mathbb{R}$ such that

$$\frac{d^2 U_n(x)}{dx^2} - \omega_n^2 U_n(x) = 0 \quad x \in (0, 1). \quad (8)$$

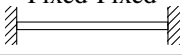

The boundary conditions of interest and the corresponding analytical modes and frequencies are summarized in Table 1. Clearly, fixed and free boundary conditions may also be mixed. The analytical frequencies appear as the roots of the frequency equation, depicted in column 3. We refer to [18, Chapter 8, Section 3] for a more detailed discussion.

From recursive application of (8) it follows that the solutions U_n to (8) are also solutions to the following higher-order eigenvalue problems,

$$\frac{d^{2+k} U_n(x)}{dx^{2+k}} - \omega_n^{2+k} U_n(x) = 0, \quad x \in (0, 1), \quad k = 0, 2, 4, \dots, \quad (9a)$$

with boundary conditions:

Table 1: Common boundary conditions for the longitudinal vibration of a bar.

End-Conditions of Bar	Boundary Conditions	Frequency Equation	Mode Shape	Natural Frequencies
Fixed-Fixed 	$u(0, t) = 0$ $u(1, t) = 0$	$\sin(\omega) = 0$	$U_n(x) = C_n \sin(\omega_n x)$	$\omega_n = n\pi$ $n = 1, 2, 3, \dots$
Free-Free 	$u_{,x}(0, t) = 0$ $u_{,x}(1, t) = 0$	$\sin(\omega) = 0$	$U_n(x) = C_n \cos(\omega_n x)$	$\omega_n = n\pi,$ $n = 0, 1, 2, \dots$ ($\omega_0 = 0$ – rigid b.m.)

1. Fixed (clamped) end:

$$\frac{d^k}{dx^k} U = 0 \quad (9b)$$

2. Free end:

$$\frac{d^{k+1}}{dx^{k+1}} U = 0 \quad (9c)$$

This observation may be verified by inspecting the analytical mode shapes listed in Table 1. Indeed, since the analytical modes are sines or cosines with homogeneous boundary conditions, their second derivatives are again sines and cosines with homogeneous boundary conditions.

3.2. Free transverse vibration of a thin Bernoulli-Euler beam

The same analysis may be applied to the free transverse vibration of a beam. Consider a uniform elastic beam of unit length with unit material properties. The normal mode W_n satisfies the eigenvalue problem: find $(W_n, \omega_n) \in \mathcal{W} \times \mathbb{R}$ such that

$$\frac{d^4 W_n(x)}{dx^4} - \omega_n^2 W_n(x) = 0 \quad x \in (0, 1). \quad (10)$$

Because (10) is a fourth-order problem, four boundary conditions need to be specified to guarantee a unique solution. Table 2 summarizes several of the common boundary conditions and the analytical modes and frequencies. Here, $\beta_n = \sqrt{\omega_n}$ are the roots of the frequency equation listed in the third column of Table 2. The first four values of β_n are listed in the fifth column with four digits of accuracy. We refer to [18, Chapter 8, Section 5] for further discussion.

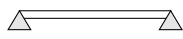
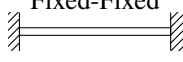

Remark 3.1. The analytical beam modes for fixed and free boundary conditions, listed in Table 2, involve hyperbolic sine and cosine functions, which are numerically unstable beyond $n = 10$. Instead, highly accurate asymptotic approximations are used, see Appendix C.

From recursive application of (10), it follows that the solutions W_n to (10) are also solutions to the following higher-order eigenvalue problems,

$$\frac{d^{4+2k} W_n(x)}{dx^{4+2k}} - \omega_n^{2+k} W_n(x) = 0, \quad x \in (0, 1), \quad k = 0, 2, 4, \dots, \quad (11a)$$

with boundary conditions:

Table 2: Common boundary conditions for the transverse vibration of a Bernoulli-Euler beam.

End-Conditions of Beam	Boundary Conditions	Frequency Equation	Mode Shape	Value of $\beta_n = \sqrt{\omega_n}$
 Pinned-Pinned	$w(0, t) = 0$	$\sin(\beta_n) = 0$	$W_n(x) = C_n \sin(\beta_n x)$	$\beta_1 = \pi$
	$w_{,xx}(0, t) = 0$			$\beta_2 = 2\pi$
	$w(1, t) = 0$			$\beta_3 = 3\pi$
	$w_{,xx}(1, t) = 0$			$\beta_4 = 4\pi$
 Fixed-Fixed	$w(0, t) = 0$	$\cos(\beta_n) \cdot \cosh(\beta_n) = 1$	$W_n(x) = C_n \{ \sinh(\beta_n x) - \sin(\beta_n x) + \alpha_n (\cosh(\beta_n x) - \cos(\beta_n x)) \}$ where $\alpha_n = \frac{\sinh(\beta_n) - \sin(\beta_n)}{\cos(\beta_n) - \cosh(\beta_n)}$	$\beta_1 = 4.7300$
	$w_{,xx}(0, t) = 0$			$\beta_2 = 7.8532$
	$w(1, t) = 0$			$\beta_3 = 10.9956$
	$w_{,xx}(1, t) = 0$			$\beta_4 = 14.1372$
 Free-Free	$w_{,xx}(0, t) = 0$	$\cos(\beta_n) \cdot \cosh(\beta_n) = 1$	$W_n(x) = C_n \{ \sinh(\beta_n x) + \sin(\beta_n x) + \alpha_n (\cosh(\beta_n x) + \cos(\beta_n x)) \}$ where $\alpha_n = \frac{\sinh(\beta_n) - \sin(\beta_n)}{\cos(\beta_n) - \cosh(\beta_n)}$	$\beta_1 = 4.7300$
	$w_{,xxx}(0, t) = 0$			$\beta_2 = 7.8532$
	$w_{,xx}(1, t) = 0$			$\beta_3 = 10.9956$
	$w_{,xxx}(1, t) = 0$			$\beta_4 = 14.1372$ ($\beta = 0$ – rigid b.m.)

1. Fixed (clamped) end:

$$\frac{d^{2k}}{dx^{2k}} W = 0 \quad (\text{Deflection}) \quad (11b)$$

$$\frac{d^{1+2k}}{dx^{1+2k}} W = 0 \quad (\text{Slope}) \quad (11c)$$

2. Simply supported (pinned) end:

$$\frac{d^{2k}}{dx^{2k}} W = 0 \quad (\text{Deflection}) \quad (11d)$$

$$\frac{d^{2k}}{dx^{2k}} M(x) = \frac{d^{2k}}{dx^{2k}} \left(\frac{d^2 W}{dx^2} \right) = 0 \quad (\text{Bending moment}) \quad (11e)$$

3. Free end:

$$\frac{d^{2k}}{dx^{2k}} M(x) = \frac{d^{2k}}{dx^{2k}} \left(\frac{d^2 W}{dx^2} \right) = 0 \quad (\text{Bending moment}) \quad (11f)$$

$$\frac{d^{2k}}{dx^{2k}} V(x) = \frac{d^{1+2k}}{dx^{1+2k}} \left(\frac{d^2 W}{dx^2} \right) = 0 \quad (\text{Shear force}) \quad (11g)$$

3.3. Multidimensional problems

This above exposition extends naturally to the multivariate setting. The resulting eigenmodes obey a similar series of eigenvalue problems with additional homogeneous boundary conditions.

130 We briefly discuss the case of a vibrating two-dimensional annular membrane. The remaining cases follow the same inductive arguments.

Consider the case of a quarter annular membrane, denoted by Ω , with fixed boundaries, see Figure 1. It is useful to consider a polar coordinate system with radial coordinate r and angular coordinate θ .

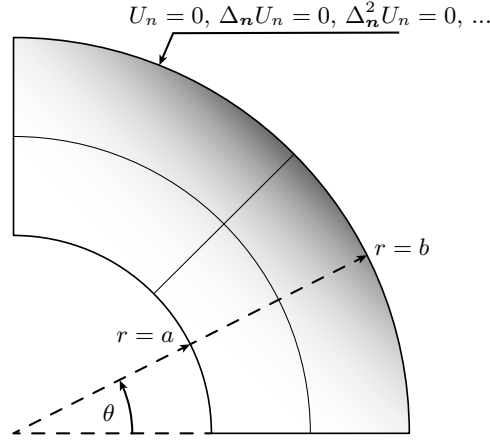


Figure 1: Quarter annular membrane with fixed boundary conditions. The eigenmodes actually satisfy additional boundary conditions involving higher order differential operators.

The eigenmodes and frequencies are governed by the eigenvalue problem

$$\Delta U_n(\mathbf{x}) - \omega_n^2 U_n(\mathbf{x}) = 0 \quad \mathbf{x} \in \Omega \quad (12a)$$

$$U_n(\mathbf{x}) = 0 \quad \mathbf{x} \in \partial\Omega. \quad (12b)$$

By the same inductive argument as before, we deduce that the eigenmodes satisfy a sequence of higher order eigenvalue problems

$$\Delta^k U_n(\mathbf{x}) - \omega_n^{2+2k} U_n(\mathbf{x}) = 0 \quad \mathbf{x} \in \Omega \quad (13a)$$

$$\Delta_n^j U_n(\mathbf{x}) = 0, \quad j = 0, 1, \dots, k-1 \quad \mathbf{x} \in \partial\Omega. \quad (13b)$$

135 where Δ_n is the part of the Laplacian operator that acts normal to the boundary. For instance, along the boundary where $r = b$ we have that $\Delta_n = \frac{\partial^2}{\partial r^2} + \frac{1}{b} \frac{\partial}{\partial r}$.

3.4. Simplifications on tensor product domains

Let d denote the spatial dimension. In Section 7, we will study the eigenvalue problem

$$\mathcal{K} U_n(\mathbf{x}) - \omega_n^2 U_n(\mathbf{x}) = 0, \quad \mathbf{x} \in (0, 1)^d, \quad (14a)$$

where \mathcal{K} is one of the following two operators:

$$\mathcal{K} := \Delta = \sum_{k=1}^d \frac{\partial^2}{\partial x_k^2} \quad (\text{Second-order operator} - d = 2, 3) \quad (14b)$$

$$\mathcal{K} := \sum_{k=1}^d \frac{\partial^4}{\partial x_k^4} \quad (\text{Fourth-order operator} - d = 2) \quad (14c)$$

The second order operator in (14b), the Laplacian, is studied in two and three space dimensions. We consider both fixed or free boundary conditions, thus generalizing the free axial vibration of a bar with the boundary conditions listed in Table 1. The fourth-order operator in (14c) is studied in two space dimensions, with fixed, simply supported, or free boundary conditions, thus generalizing free vibration of a beam with the boundary conditions listed in Table 2.

We note that since $\sum_k \frac{\partial^4}{\partial x_k^4} \neq \Delta^2$, the fourth-order operator in (14c) does not describe exactly the behavior of a thin plate. Our choice deserves some explanation. The analytical solution of a thin plate, governed by the bi-harmonic operator $\mathcal{K} = \Delta^2$, is well known only in the case of simply supported boundary conditions, see [19]. As we are also interested in cases with free and fixed boundary conditions, we have chosen to investigate the spectra of the similar fourth-order operator in (14c), for which we can derive analytical solutions.

Due to the simple structure of \mathcal{K} in both (14b) and (14c), the analytical solution to the eigenvalue problem in (14a) may be obtained using separation of variables, and can be conveniently represented in terms of the analytical frequencies ω_n and modes $U_n(x)$ in Tables 1 and 2, respectively. In multi-index notation, $n = (m, n)$ in 2d, and $n = (m, n, o)$ in 3d, we have

$$\omega_{mn} = \sqrt{\omega_m^2 + \omega_n^2} \quad U_{mn}(x, y) = U_m(x) \cdot U_n(y) \quad (15a)$$

$$\omega_{mno} = \sqrt{\omega_m^2 + \omega_n^2 + \omega_o^2} \quad U_{mno}(x, y, z) = U_m(x) \cdot U_n(y) \cdot U_o(z). \quad (15b)$$

4. Characterization of outlier frequencies and modes

Based on empirical results, we first provide the number of outliers that appear for discretizations of second- and fourth-order problems in one spatial dimension. Our counts are functions of the polynomial degree and the type of imposed boundary conditions. We then generalize our counts to tensor-product discretizations. We start with an example to give an intuitive idea of what the outliers look like and what properties they have.

4.1. A one-dimensional example

Consider the natural vibrations of a fixed bar represented by the eigenvalue problem in (8) with “fixed-fixed” boundary conditions depicted in Table 1. Let $\mathcal{U}^h \subset \mathcal{U}$ denote a trial space of smooth C^3 splines of polynomial degree $p = 4$, defined on 20 uniform elements. Suppose the eigenvalue problem is discretized using the Galerkin method, where the consistent mass matrix is used.

Figure 2 depicts the 22 calculated discrete eigenfrequencies. We observe that all frequencies are reasonably accurate except for the last two, which significantly overestimate the true frequencies. By inspection of the corresponding mode shapes, mode 21 and 22 in Figure 3, it becomes clear that these modes and corresponding frequencies are spurious, that is, they behave very differently from the exact sinusoidal mode shapes and hence can be considered numerical artifacts.

4.2. Outlier modes and frequencies of univariate discretizations

Higher-order discretizations feature additional outliers, and they seem more pronounced for free boundary conditions than for fixed ones. Our observations suggest that in all cases, the outlier modes emanate from boundaries (at least in the setting of smooth C^{p-1} splines), with most of their

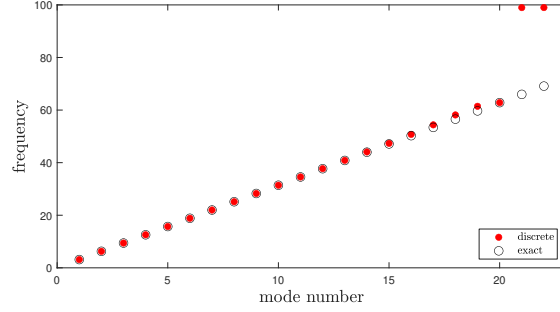


Figure 2: Discrete frequencies representing the natural vibration of a fixed bar computed with C^3 splines of polynomial order $p = 4$ on 20 uniform elements. The two outliers at the end significantly overestimate the true frequencies.

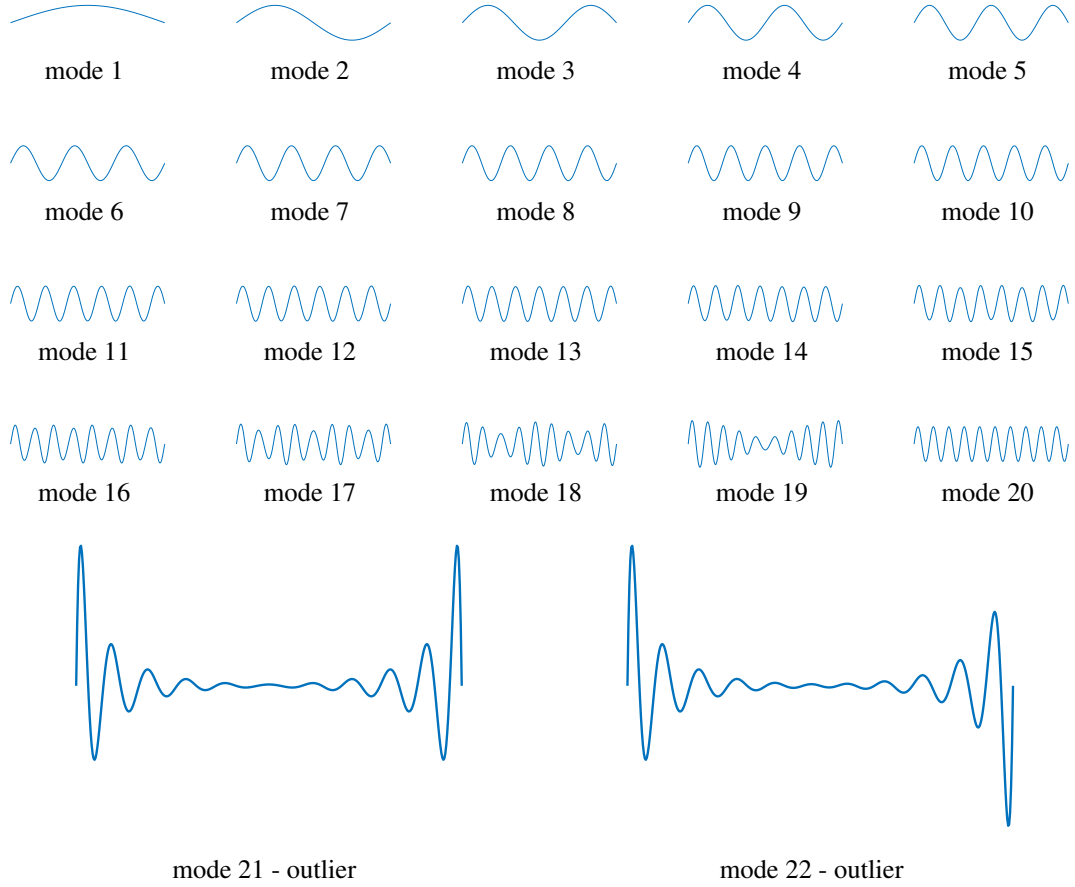


Figure 3: Discrete modes, corresponding to the discrete frequencies in Figure 2, approximating the exact modes $\sin(\pi \cdot n)$, $n = 1, 2, \dots, 22$. Mode 21 and 22, corresponding to the two outlier frequencies in Figure 2, are spurious, as their behavior differs significantly from the exact sinusoidal modes $\sin(21\pi x)$ and $\sin(22\pi x)$.

energy located near boundaries, and involve sharp higher-order derivatives, again near boundaries. Section 6 lists the spectral results obtained for univariate second- and fourth-order problems. Here, we provide a summary of some key observations with regard to the number of outliers. Table 3 and 4 list the number of outliers as a function of polynomial degree and imposed boundary condition. We clearly observe that in the case of free boundary conditions, outliers occur already at degree two, and, at equal p , there are more outliers than for the other boundary conditions.

Table 3: Number of spurious outlier modes for axial vibration of a bar




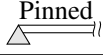
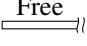
polynomial degree	2	3	4	5	6	p
 Fixed	0	1	1	2	2	$\lfloor \frac{p-1}{2} \rfloor$
 Free	1	1	2	2	3	$\lfloor \frac{p}{2} \rfloor$

Table 4: Number of spurious outlier modes for transverse vibration of a beam

polynomial degree	2	3	4	5	6	p
 Fixed	0	0	1	1	2	$\lfloor \frac{p-2}{2} \rfloor$
 Pinned	0	1	1	2	2	$\lfloor \frac{p-1}{2} \rfloor$
 Free	1	1	2	2	3	$\lfloor \frac{p}{2} \rfloor$

Remark 4.1. Tables 3 and 4 list the number of outliers associated with the left boundary only. The total number of outliers is obtained by inspecting and adding the values corresponding to the right boundary. For example, a beam fixed at the left and pinned at the right has one outlier for degree $p = 3$, two for $p = 4$ and three for $p = 5$.

4.3. Outlier modes and frequencies of multivariate tensor product discretizations

Multivariate discretizations based on tensor-products suffer much more from spurious outlier modes. Due to the tensor-product structure, there are spurious outlier modes associated with the corners of the domain, the boundary edges, and, in three dimensions, with the boundary faces of the domain. Based on the numbers obtained in the one-dimensional case, we can exactly predict how many outliers exist in multivariate tensor-product meshes.

Let \mathcal{V}^h denote a univariate trial space of dimension n with appropriate built-in boundary conditions (fixed, simply supported, free). The one-dimensional univariate discretization contains n

modes, of which \hat{n} are regular and $2k$ are spurious (k associated with each boundary). In multi-variate tensor-product discretizations, we can count the modes as follows:

$$n^2 = (\hat{n} + 2k)^2 = \hat{n}^2 + 4k\hat{n} + 4k^2 \quad \text{2D: } \mathcal{V}^h \otimes \mathcal{V}^h \quad (16)$$

$$n^3 = (\hat{n} + 2k)^3 = \hat{n}^3 + 6k\hat{n}^2 + 12k^2\hat{n} + 8k^3 \quad \text{3D: } \mathcal{V}^h \otimes \mathcal{V}^h \otimes \mathcal{V}^h \quad (17)$$

185 In two-dimensional bi-variate tensor-product discretizations, outlier modes (all terms that involve k) can be attributed to the four edges and four corners. In three-dimensional tri-variate tensor-product discretizations, additional outlier modes are associated with the six faces, twelve edges and eight corners. Figures 4 and 5 illustrate the percentage of the spectrum that is negatively affected by outliers in bi-variate and tri-variate tensor-product discretizations, respectively. For
 190 example, in bi-variate discretization using 20×20 nodes, 18% of the spectrum is dominated by edge outliers and 1% by corner outliers at $k = 1$. These numbers rise to approximately 32% and 4%, respectively, for $k = 2$, and decrease with mesh resolution. In three dimensions, the situation is worse, see Figure 5. On $20 \times 20 \times 20$ meshes, with $k = 1$, the discrete spectra are polluted by approximately 24% face outliers, 3% edge outliers and 0.1% corner outliers. These numbers grow to 38%, 10% and 0.8%, respectively, when $k = 2$.
 195

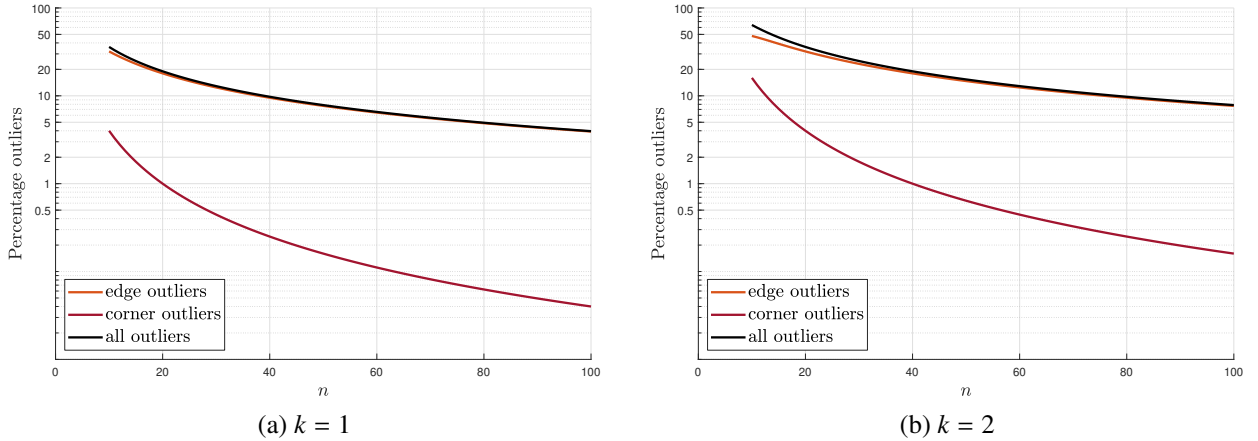


Figure 4: Fraction of corner and edge outliers with respect to the total number of modes in bi-variate $n \times n$ tensor-product discretizations.

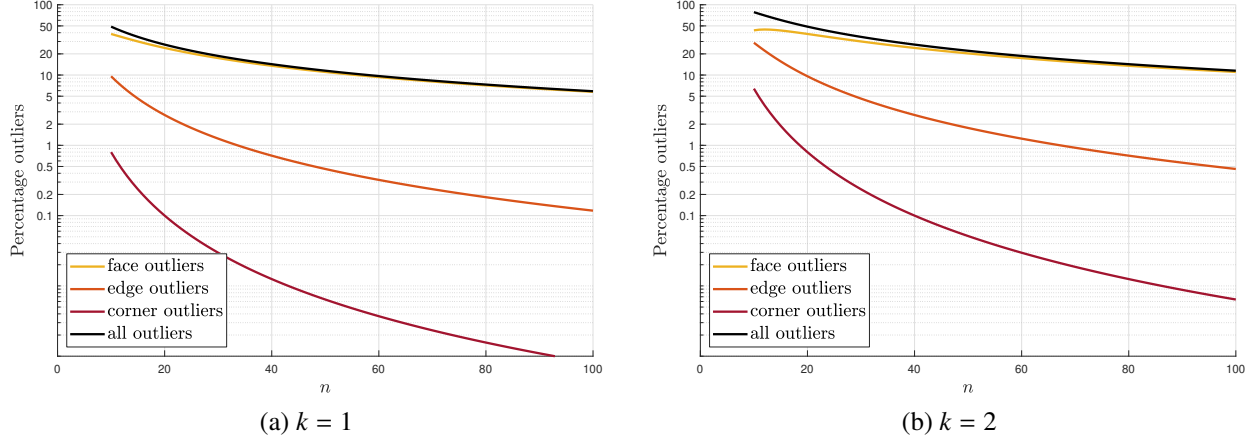


Figure 5: Fraction of corner, edge, and face outliers with respect to the total number of modes in tri-variate $n \times n \times n$ tensor-product discretizations.

5. Outlier-free extraction operator

In this section, we introduce a linear subspace of splines that incorporates additional homogeneous boundary constraints. A basis for this subspace is determined in terms of a linear combination of B-splines. We start this section with a brief recap of univariate B-splines.

5.1. Univariate B-splines

A spline is a piecewise polynomial that is characterized by the polynomial degree of its segments and the prescribed regularity at their interfaces. Let \mathcal{P}^p denote the space of piecewise polynomials of total degree $p \geq 0$ and consider a partitioning of $[a, b] \subset \mathbb{R}$ into an increasing sequence of *breakpoints*,

$$a = t_0 < \dots < t_{k-1} < t_k < \dots < t_m = b \quad (18)$$

The space of smooth C^{p-1} splines is defined as

$$\mathbb{S} = \left\{ s : [a, b] \mapsto \mathbb{R} : s|_{(t_{k-1}, t_k)} \in \mathcal{P}^p \text{ and } s \text{ is } C^{p-1} \text{ smooth at } x = t_1, \dots, t_{m-1} \right\} \quad (19)$$

Let $(B_i, i = 1, \dots, n)$ denote the degree p univariate B-splines defined on the partition in (18) with C^{p-1} continuity at the internal breakpoints and with interpolating end-conditions³. B-splines have important mathematical properties, many of which are useful in design as well as in analysis. Smooth B-splines reproduce polynomials, have built-in C^{p-1} continuity, provide a positive partition of unity and form a basis for \mathbb{S} .

³This means that the B-splines are defined on an open knotvector, see [20].

5.2. Outlier-free linear subspace \mathbb{S}^-

We shall develop a special linear subspace of splines that satisfies additional homogeneous constraints on certain derivatives at the boundary:

$$\mathbb{S}^- := \left\{ s \in \mathbb{S} : g_\alpha(s)|_{x=a} = 0 \text{ for } \alpha \in \mathcal{A}, \text{ and } g_\beta(s)|_{x=b} = 0 \text{ for } \beta \in \mathcal{B} \right\}. \quad (20)$$

Here $g_\alpha(s)$ denotes a differential operator of order α , that is, $g_\alpha(s) = \sum_{k=0}^{\alpha} \gamma_k D^k s(x)$ for some coefficients γ_k , $k = 0, 1, \dots, \alpha$, and \mathcal{A} and \mathcal{B} denote index sets that depend on the problem type and on the type of boundary condition that is implemented.

210 In the case of **2nd-order problems**:

- 1 Fixed (clamped) end: $\mathcal{A} = \{(0), 2, 4, 6, \dots, p-1\}$ with

$$g_\alpha(s) := \Delta_n^{\frac{\alpha}{2}}(s) \quad (21a)$$

- 2 Free end: $\mathcal{A} = \{1, 3, 5, \dots, p-1\}$ with

$$g_\alpha(s) := \Delta_n^{\frac{\alpha-1}{2}}\left(\frac{\partial s}{\partial x}\right) \quad (21b)$$

In the case of **4th-order problems**:

- 1 Fixed (clamped) end: $\mathcal{A} = \{(0), (1), 4, 5, 8, 9, \dots, p-1\}$ with

$$g_\alpha(s) := \begin{cases} \Delta_n^{\frac{\alpha}{2}}(s), & \alpha \text{ is even} \\ \Delta_n^{\frac{\alpha-1}{2}}\left(\frac{\partial s}{\partial x}\right), & \alpha \text{ is odd} \end{cases} \quad (22a)$$

- 2 Simply supported (pinned) end: $\mathcal{A} = \{(0), 2, 4, 6, \dots, p-1\}$ with

$$g_\alpha(s) := \Delta_n^{\frac{\alpha}{2}}(s) \quad (22b)$$

- 3 Free end: $\mathcal{A} = \{2, 3, 6, 7, \dots, p-1\}$ with

$$g_\alpha(s) := \begin{cases} \Delta_n^{\frac{\alpha}{2}}(s), & \alpha \text{ is even} \\ \Delta_n^{\frac{\alpha-1}{2}}\left(\frac{\partial s}{\partial x}\right), & \alpha \text{ is odd} \end{cases} \quad (22c)$$

Here Δ_n denotes the normal component of the Laplacian operator. The constraints are chosen such that the higher-order derivatives in (9) and (11) are constrained to zero at the boundary. In the one-dimensional case we simply have that $\Delta_n = D^2$. In the multidimensional setting with curved boundaries things are more complicated. For example, in case of an annulus in polar coordinates (r, θ) we have that the normal component of the Laplacian is $\Delta_n := D^2 + \frac{1}{r}D$.

Remark 5.1. The boundary constraints given by the problem formulation are not built into \mathbb{S}^- , but applied later in the usual way. This pertains to constraints that correspond to index $\alpha, \beta = 0$ for a fixed end of a bar and a simply supported end of a beam, and, in addition, to $\alpha, \beta = 1$ for the fixed end of a beam.

5.3. A basis for \mathbb{S}^-

Since \mathbb{S}^- is a subspace of \mathbb{S} , it is possible to construct a basis for \mathbb{S}^- in terms of linear combinations of B-splines. To achieve this, we construct ‘new’ spline basis functions

$$\hat{B}_j(x) := \sum_{i=1}^n B_i(x) C_{ij}, \quad j = 1, 2, \dots, \hat{n} \quad (23)$$

in such a way that $(\hat{B}_j, j = 1, 2, \dots, \hat{n})$ is a basis for \mathbb{S}^- with the following properties:

$$g_\alpha(\hat{B}_j)|_{x=a} = 0 \quad \text{for all } \alpha \in \mathcal{A} \quad (\text{Boundary constraint at } x = a) \quad (24a)$$

$$g_\beta(\hat{B}_j)|_{x=b} = 0 \quad \text{for all } \beta \in \mathcal{B} \quad (\text{Boundary constraint at } x = b) \quad (24b)$$

$$\sum_j \hat{B}_j(x) = 1 \quad \text{for all } x \in [a, b] \quad (\text{Partition of unity}) \quad (24c)$$

$$\hat{B}_j(x) \geq 0 \quad \text{for all } x \in [a, b] \quad (\text{Non-negativity}) \quad (24d)$$

$$\hat{B}_j \text{ has minimal compact support} \quad (24e)$$

It can be shown via the theory laid out in [15, 16] that these properties uniquely define the entries in matrix \mathbf{C} . Firstly, \mathbf{C} is a basis for the null-space of a matrix $\mathbf{A} \in \mathbb{R}^{r \times n}$, with $r = |\mathcal{A}| + |\mathcal{B}|$, whose rows correspond to a constraint in (24a) or (24b). In particular, under the assumption that the two boundary constraints are well separated, that is, they do not interfere with one another, matrix \mathbf{A} is

$$\mathbf{A} = \begin{bmatrix} \mathbf{A}_L & 0 & 0 \\ 0 & 0 & \mathbf{A}_R \end{bmatrix} \quad (25a)$$

with

$$[\mathbf{A}_L]_{ij} = g_{\mathcal{A}(i)}(B_j(a)) \quad (25b)$$

$$[\mathbf{A}_R]_{ij} = g_{\mathcal{B}(i)}(B_{n-p+j}(b)) \quad (25c)$$

Matrix \mathbf{A}_L can be computed by considering only the first p B-splines. Analogously, matrix \mathbf{A}_R can be computed by considering only the last p B-splines.

Since the constraints are linearly independent, we seek a full rank matrix \mathbf{C} (such that $\mathbf{AC} = 0$) of size $n \times \hat{n}$, with $\hat{n} = n - r$. Due to the special structure of \mathbf{A} , matrix \mathbf{C} has the special structure

$$\mathbf{C} = \begin{bmatrix} \mathbf{C}_L & 0 & 0 \\ 0 & \mathbf{I} & 0 \\ 0 & 0 & \mathbf{C}_R \end{bmatrix} \quad (26)$$

The requirement that $\mathbf{AC} = 0$ implies that \mathbf{C}_L and \mathbf{C}_R satisfy, respectively, $\mathbf{A}_L \mathbf{C}_L = 0$ and $\mathbf{A}_R \mathbf{C}_R = 0$. These conditions imply that the properties (24a) and (24b) are satisfied.

Next, partition of unity (24c) implies that the rows of \mathbf{C} sum to one. Property (24d) implies that \mathbf{C} has non-negative entries only. Since B-splines have minimal compact support, and the new functions are combinations of B-splines, it follows from property (24e) that \mathbf{C} is ultimately sparse

and banded. The matrix structure of \mathbf{C} implies that these requirements can be directly applied to matrices \mathbf{C}_L and \mathbf{C}_R .

Algorithms 1 and 2, given in Appendix A, compute the matrices \mathbf{C}_L or \mathbf{C}_R , given \mathbf{A}_L and \mathbf{A}_R as input, respectively. Instead of providing a complete theoretical derivation of the construction of the basis functions, which follows the above sketched approach and the theoretical arguments in the above cited sources, we provide a worked-out example that illustrates how matrix \mathbf{C} is computed in practice.

Example 5.2 (Computation of extraction operator). *Consider free vibrations of a bar with fixed (clamped) boundary conditions specified at the left boundary $x = 0$ and free boundary conditions specified at the right boundary $x = 1$. Let $\mathbb{S}(0, 1)$ denote a C^3 quartic spline space defined on a partition $(0.0, 0.2, 0.4, 0.6, 0.8, 1.0)$.*

Matrices \mathbf{A}_L in (25b) and \mathbf{A}_R in (25c) are computed as

$$[\mathbf{A}_L]_{ij} = D^{\mathcal{A}(i)}(B_j(0)) = \begin{bmatrix} 300 & -450 & 150 & 0 \end{bmatrix}$$

$$[\mathbf{A}_R]_{ij} = D^{\mathcal{B}(i)}(B_{n-p+j}(1)) = \begin{bmatrix} 0 & 0 & -20 & 20 \\ -500 & 2750 & -5250 & 3000 \end{bmatrix}$$

The matrix \mathbf{C}_L is computed using a single pass of Algorithm 2 as

$$\mathbf{C}_L = \begin{bmatrix} 1 & 0 & 0 \\ 2/3 & 1/3 & 0 \\ 0 & 1 & 0 \\ 0 & 0 & 1 \end{bmatrix}$$

It can be readily verified that $\mathbf{A}_L \mathbf{C}_L = \mathbf{0}$. Furthermore, \mathbf{C}_L is clearly of full rank and, hence, its columns span the null-space of \mathbf{A}_L . Computing \mathbf{C}_R requires two passes of Algorithm 2. We have that

$$\mathbf{C}_{R1} = \begin{bmatrix} 1 & 0 & 0 \\ 0 & 1 & 0 \\ 0 & 0 & 1 \\ 0 & 0 & 1 \end{bmatrix} \Rightarrow \mathbf{A}_R \mathbf{C}_{R1} = \begin{bmatrix} 0 & 0 & 0 \\ -500 & 2750 & -2250 \end{bmatrix} \Rightarrow \mathbf{C}_{R2} = \begin{bmatrix} 1 & 0 \\ 2/11 & 9/11 \\ 0 & 1 \end{bmatrix}$$

which results in

$$\mathbf{C}_R = \mathbf{C}_{R1} \mathbf{C}_{R2} = \begin{bmatrix} 1 & 0 \\ 2/11 & 9/11 \\ 0 & 1 \\ 0 & 1 \end{bmatrix}$$

It can be readily verified that $\mathbf{A}_R \mathbf{C}_R = \mathbf{0}$. Like before, the matrix \mathbf{C}_R is of full rank by construction and, consequently, the columns of \mathbf{C}_R are a basis for the null-space of \mathbf{A}_R .

The final matrix is composed of the individual sub-matrices and is given below. Since all rows of \mathbf{C} sum to one, the basis for \mathbb{S}^- retains partition of unity. Furthermore, by construction

all entries are positive and ultimately sparse leading to positive basis functions with minimum compact support.

$$\mathbf{C} = \left[\begin{array}{ccc|c|cc} 1 & 0 & 0 & 0 & 0 & 0 \\ 2/3 & 1/3 & 0 & 0 & 0 & 0 \\ 0 & 1 & 0 & 0 & 0 & 0 \\ 0 & 0 & 1 & 0 & 0 & 0 \\ \hline 0 & 0 & 0 & 1 & 0 & 0 \\ \hline 0 & 0 & 0 & 0 & 1 & 0 \\ 0 & 0 & 0 & 0 & 2/11 & 9/11 \\ 0 & 0 & 0 & 0 & 0 & 1 \\ 0 & 0 & 0 & 0 & 0 & 1 \end{array} \right]$$

The quartic basis functions for the reduced spaces, computed in the above example, are depicted in Figure 6. We observe that the original B-splines plotted in the left column exhibit higher derivatives whose absolute values are significantly larger at the boundaries than within the domain. In contrast, the higher derivatives of the new basis functions plotted in the right column assume similar absolute values across the entire domain. The change in derivative behavior provides a first indication for the improved spectral behavior of the new basis.

5.4. Tensor product spaces

In this paper we consider extensions to multivariate splines by means of the tensor product. All spectral analysis experiments presented in Section 7 are performed by applying the same discretization in every coordinate direction. The multivariate spaces encountered are $\mathbb{S}^- \otimes \mathbb{S}^- \subset \mathbb{S} \otimes \mathbb{S}$ and $\mathbb{S}^- \otimes \mathbb{S}^- \otimes \mathbb{S}^- \subset \mathbb{S} \otimes \mathbb{S} \otimes \mathbb{S}$. The tensor product structure leads to matrices with Kronecker structure in cases the parametric mapping is affine, see Appendix D.

5.5. Mapped geometry

To illustrate how the geometrical mapping has an effect on the applied constraints we investigate the case of a quarter annular membrane, denoted by Ω , with inner radius a and outer radius b . It is useful to consider a polar coordinate system with radial coordinate r and angular coordinate θ . Let $\Phi : [a, b] \times [0, \pi/2] \mapsto \Omega \subset \mathbb{R}^2$ denote the mapping from parametric space to the quarter annulus in \mathbb{R}^2 , see Figure 7.

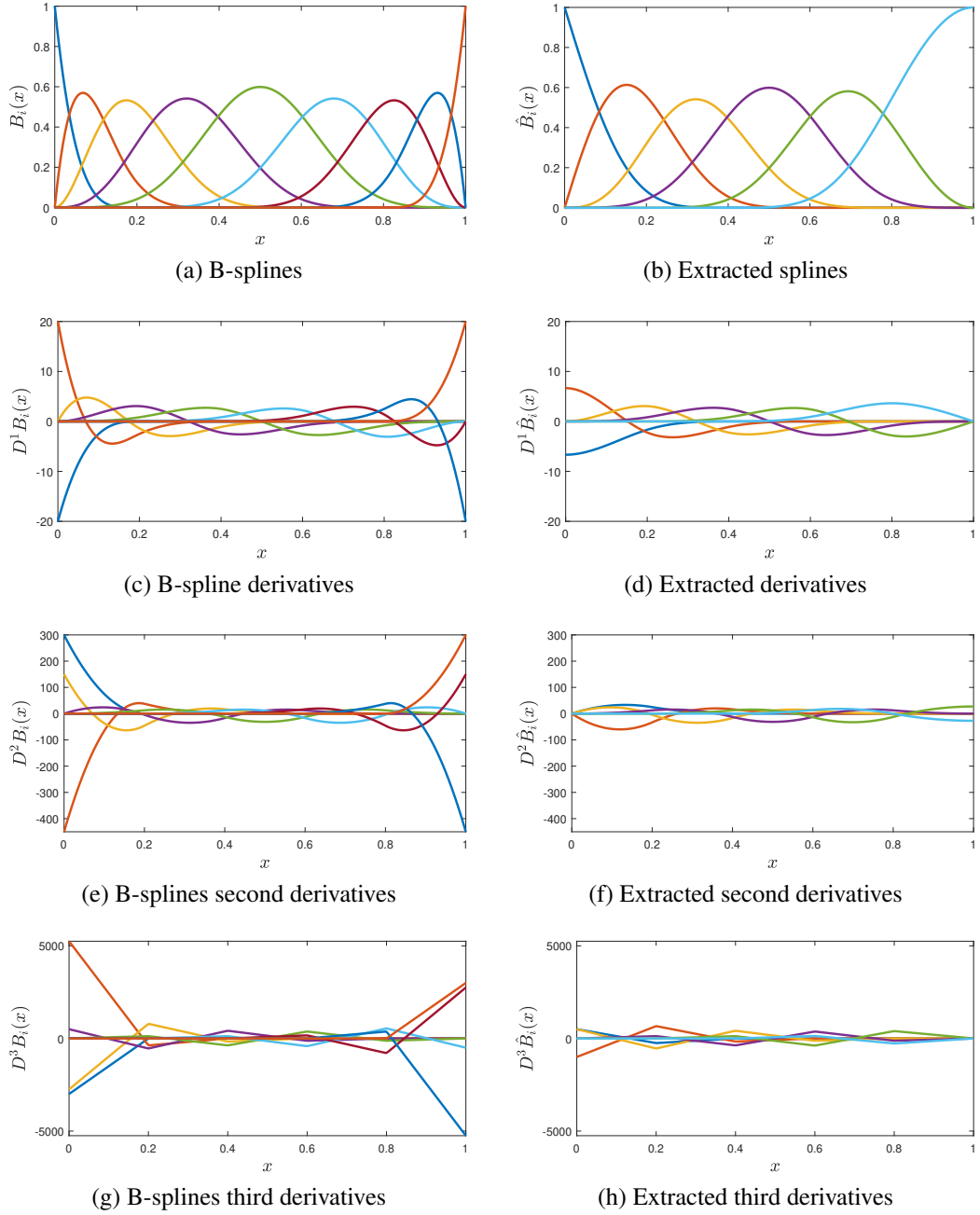


Figure 6: C^3 smooth quartic B-splines (left column) and extracted splines (right column) defined on the partition $(0.0, 0.2, 0.4, 0.6, 0.8, 1.0)$ corresponding to Example 5.2. Note that the derivatives of the extracted splines are much better behaved near the boundary than the ones of the B-splines.

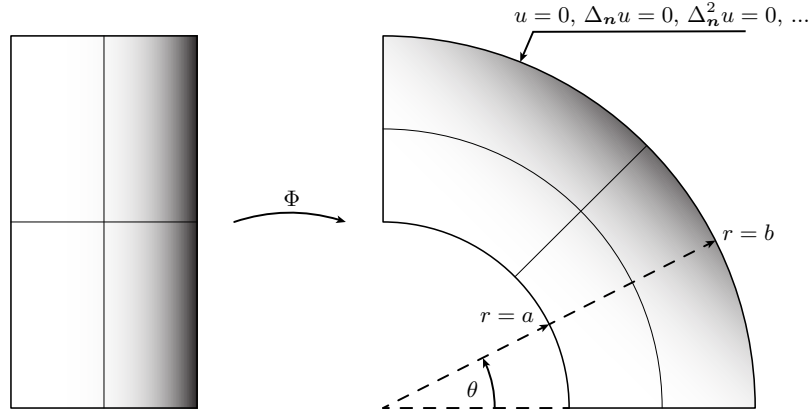


Figure 7: Mapping from rectangular parametric domain to a quarter annulus.

We consider the case of a membrane with fixed boundary conditions on all sides. A space of splines can be constructed on the parametric domain $[a, b] \times [0, \pi/2]$

$$\mathbb{S}^-(a, b) \otimes \mathbb{S}^-(0, \pi/2)$$

and pushed forward to Ω by means of the mapping Φ . As an example we discuss the constraints at the outer boundary where $r = b$. The Laplacian in polar coordinates is $\Delta = \frac{\partial^2}{\partial r^2} + \frac{1}{r} \frac{\partial}{\partial r} + \frac{1}{r^2} \frac{\partial^2}{\partial \theta^2}$ and its radial component is $\Delta_n = \frac{\partial^2}{\partial r^2} + \frac{1}{r} \frac{\partial}{\partial r}$. The first three constraints for any $u \in \mathbb{S}^-(a, b) \otimes \mathbb{S}^-(0, \pi/2)$ at the boundary at $r = b$ are

$$u|_{r=b} = 0 \quad (\text{essential boundary condition}) \quad (27a)$$

$$\Delta_n u|_{r=b} = \frac{\partial^2 u}{\partial r^2} + \frac{1}{r} \frac{\partial u}{\partial r} \Big|_{r=b} = 0 \quad (1^{\text{st}} \text{ constraint for } p > 2) \quad (27b)$$

$$\Delta_n^2 u|_{r=b} = \frac{\partial^4 u}{\partial r^4} + \frac{2}{r} \frac{\partial^3 u}{\partial r^3} - \frac{1}{r^2} \frac{\partial^2 u}{\partial r^2} + \frac{1}{r^3} \frac{\partial u}{\partial r} \Big|_{r=b} = 0 \quad (2^{\text{nd}} \text{ constraint for } p > 4) \quad (27c)$$

Because the radius of curvature is constant along the outer boundaries, the constraints do not change along the sides of the boundary. Therefore the constraint spline space admits a tensor product structure. For general mappings this is no longer the case and, consequently, the boundary conditions no longer admit a tensor-product structure. We postpone this more general setting to future work.

6. One-dimensional study of spectra and modes

We investigate the spectral properties of the reduced spline basis, developed in the previous section, applied to problems with second- and fourth-order operators in one spatial dimension. We consider the free axial vibration of a bar with fixed and free boundary conditions, and the free transverse vibration of a beam with fixed, simply supported, and free boundary conditions. The study is performed for polynomial degrees $p = 2 - 5$ and all cases where outliers exist, see Tables 3 and 4.

6.1. Presentation of the data

The figures on the following pages present the normalized errors made in the univariate frequencies and mode shapes. The graphs contain several levels of detail. For a better understanding, we briefly summarize their main attributes.

- Each row corresponds to results obtained with a fixed polynomial degree, ranging from $p = 3$ to $p = 5$ for fixed boundary conditions, and $p = 2$ to $p = 4$ for free boundary conditions, in those cases where there are outliers.
- The left column displays the normalized frequency error (Equation (6a)) as a function of the normalized mode number, n/N . Results with the outlier-free basis (yellow) are directly compared with standard B-splines (black) for $N = 1000$.
- The right column displays the normalized L^2 error in the mode shapes (Equation (6b)) as a function of the normalized mode number, n/N . Results with the outlier-free basis (yellow) are directly compared with standard B-splines (black) for $N = 1000$.
- The inset figures with semi-log axes in the left and right column focus on the error made in the first five frequencies and modes, respectively, obtained on meshes using $N = 10$ and $N = 20$ degrees of freedom. The results denoted with the symbol “o” are obtained with B-splines and serve as the reference values. The results denoted with the “+” symbol refer to those results obtained with the outlier-free basis.
- The remaining inset figure in the left column focuses on the last five frequencies, and illustrates, in particular, the behavior of the outliers.

6.2. Second-order eigenvalue problems: free axial vibration of a bar

Figures 8 and 9 illustrate the normalized frequency and modal errors corresponding to the free vibration of a bar with fixed and free boundary conditions, respectively. It can be observed that all frequencies obtained with B-splines (in black) are accurate except for a few outlier frequencies. These are eliminated using the outlier-free basis (yellow), without affecting the remaining frequencies. In fact, in many cases the frequencies and modes are not only more accurate in the upper part, but also in low part, which is particularly important for the accuracy of a discretization. We observe that this is particularly true for coarse meshes, which can be seen from the inset figure of the first five frequencies and modes. We conclude that accurate results are obtained for both fixed and free boundary conditions.

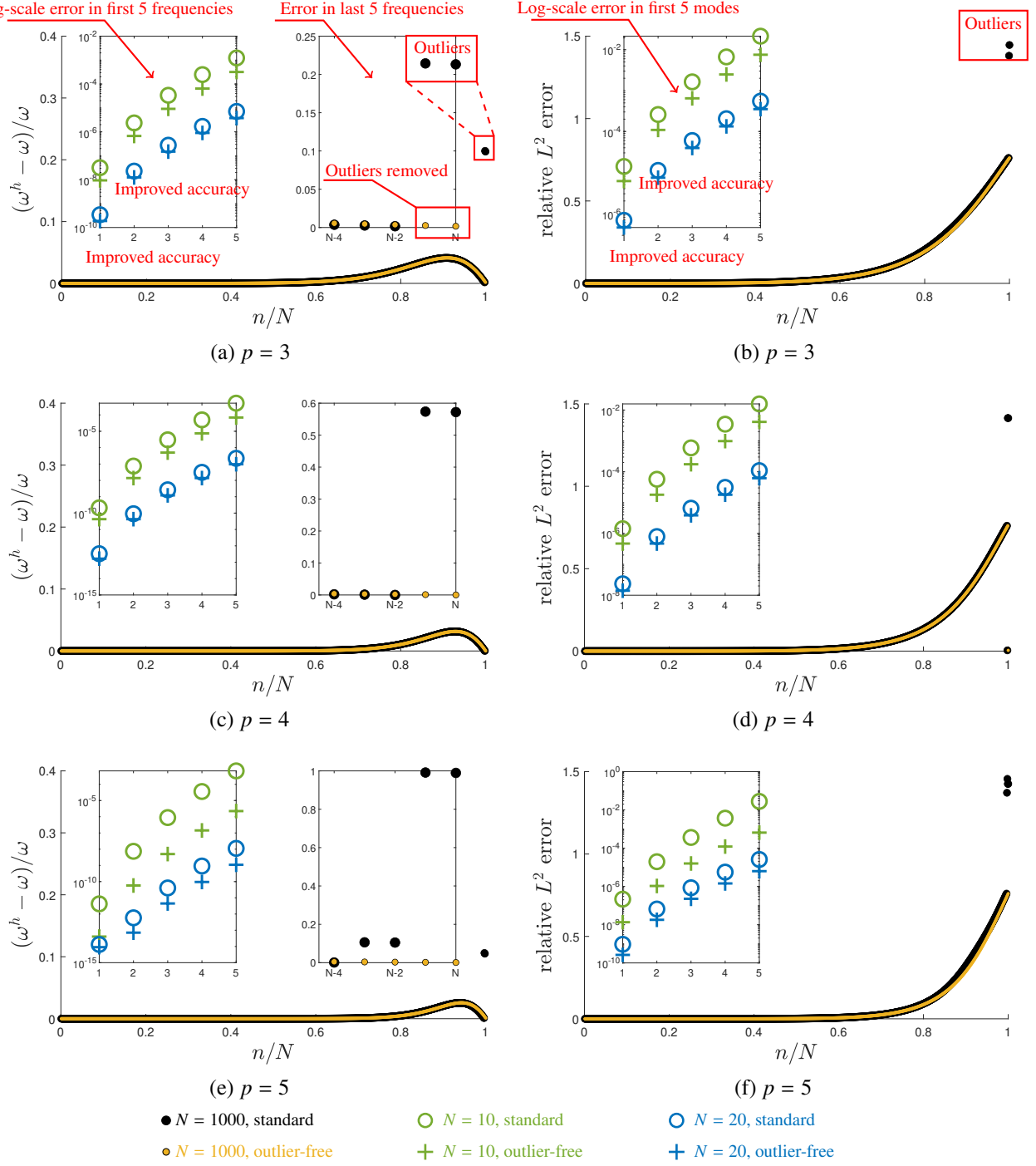


Figure 8: **Normalized frequency error (left) and L^2 errors in the mode shapes (right) of the free vibration of a bar with fixed boundary conditions.** The three inset figures show, from left to right, the normalized errors in the first five frequencies, the normalized errors in the last five frequencies, and the relative L^2 errors in the first five modes.

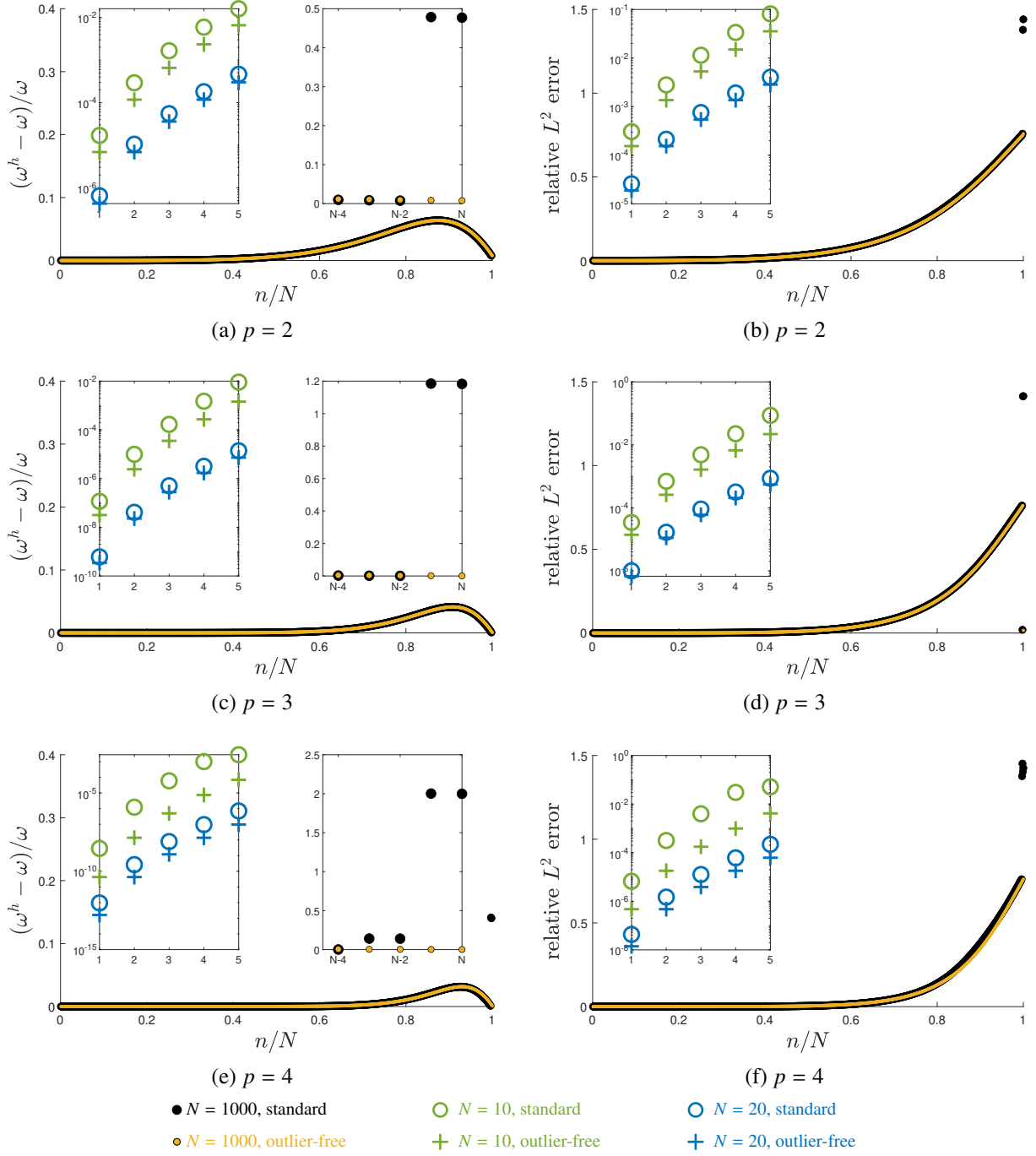


Figure 9: **Normalized frequency error (left) and L^2 errors in the mode shapes (right) of free vibration of a bar with free boundary conditions.** The three inset figures show, from left to right, the normalized errors in the first five frequencies, the normalized errors in the last five frequencies, and the relative L^2 errors in the first five modes.

6.3. Fourth-order eigenvalue problems: free transverse vibration of a beam

The outlier-free basis also yields accurate results in eigenvalue problems corresponding to fourth-order operators in one spatial dimension, see Figures 10, 11 and 12. Similar conclusions may be drawn as in the case of second-order operators in the previous subsection. We note that odd degrees perform better than even degrees, particularly in combination with fixed and free boundary conditions. Nevertheless, outliers are successfully removed in all cases, and improved accuracy is attained over a significant portion of the modes.

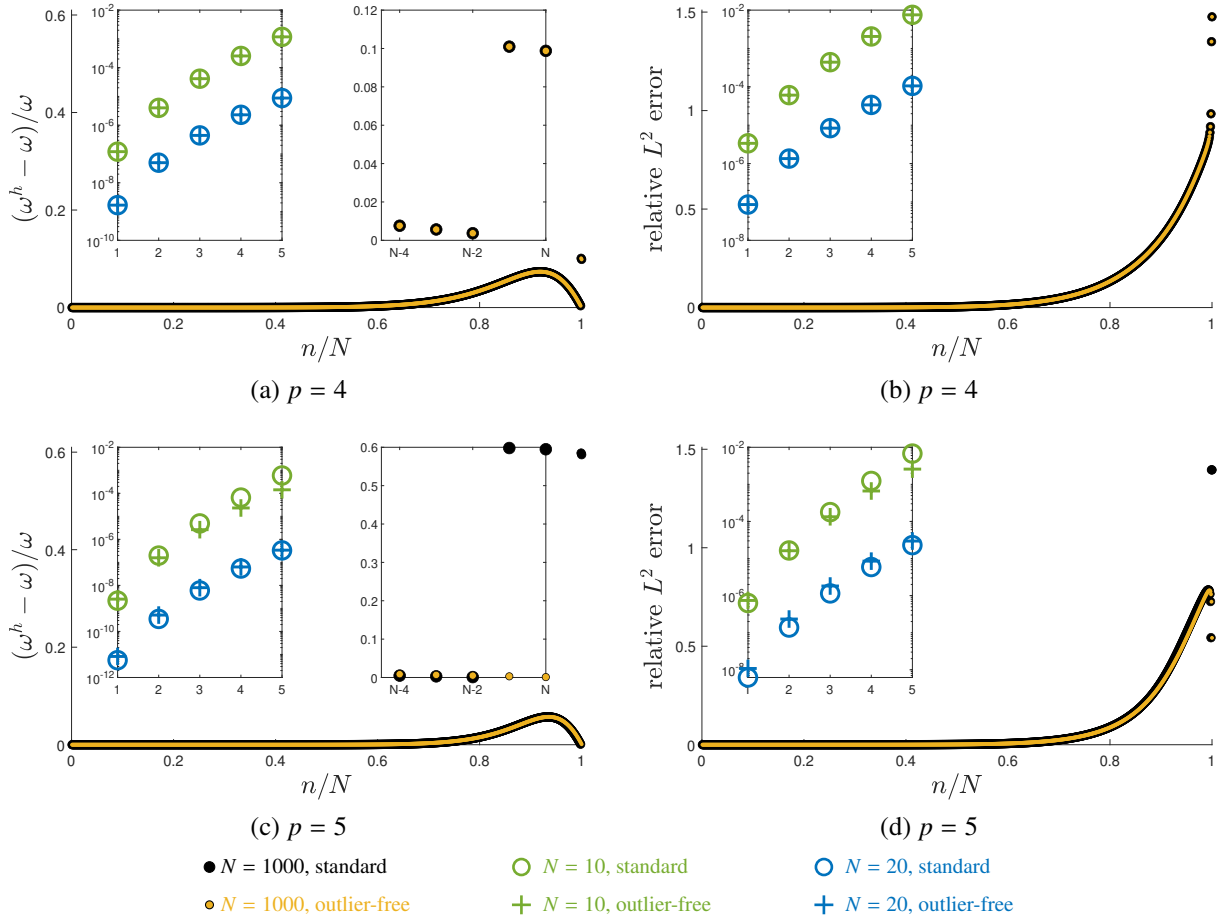


Figure 10: **Normalized frequency error (left) and L^2 errors in the mode shapes (right)** of the free vibration of a beam with fixed boundary conditions. The three inset figures show, from left to right, the normalized errors in the first five frequencies, the normalized errors in the last five frequencies, and the relative L^2 errors in the first five modes.

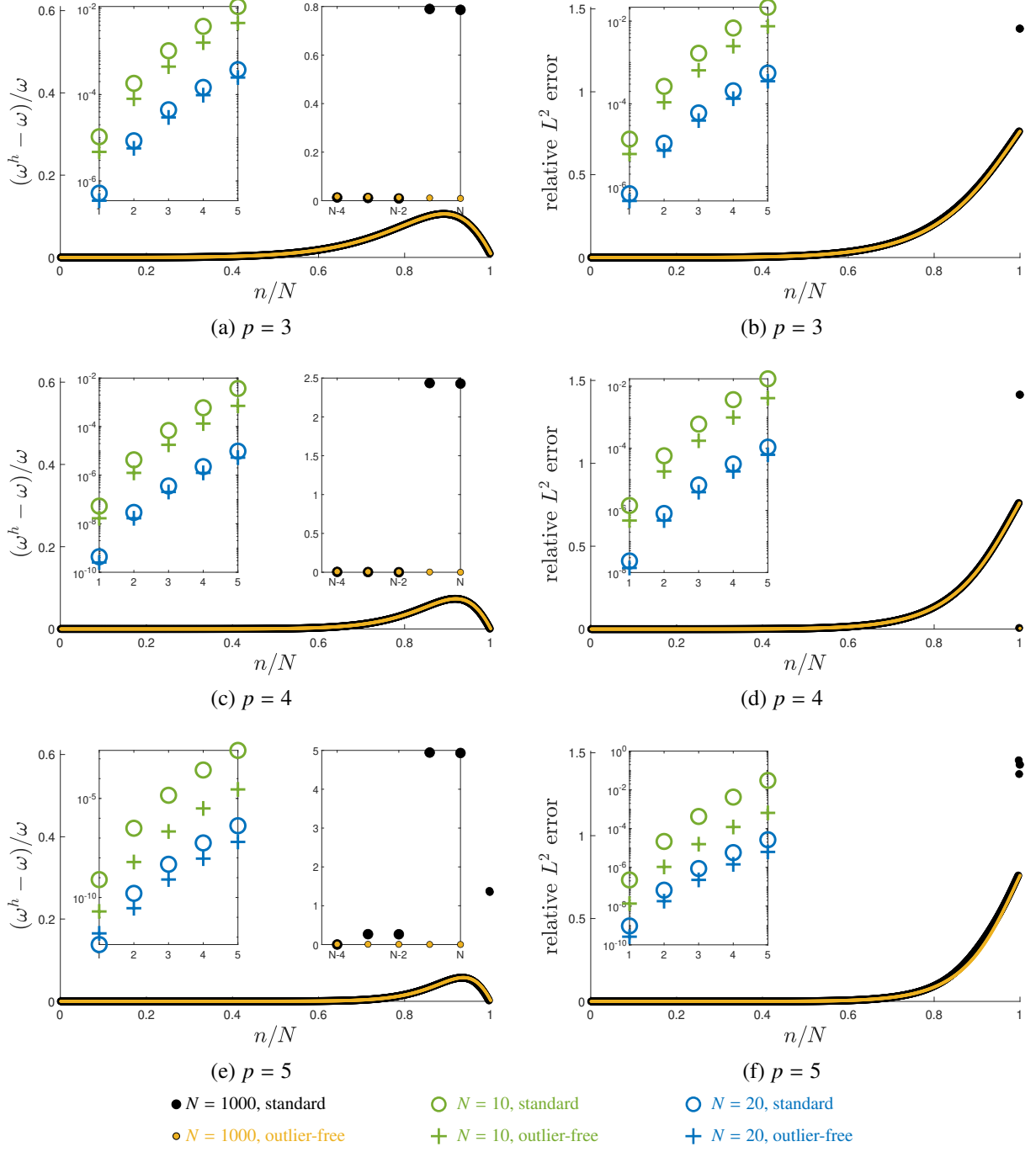


Figure 11: **Normalized frequency error (left) and L^2 errors in the mode shapes (right) of the free vibration of a beam with simply-supported boundary conditions.** The three inset figures show, from left to right, the normalized errors in the first five frequencies, the normalized errors in the last five frequencies, and the relative L^2 errors in the first five modes.

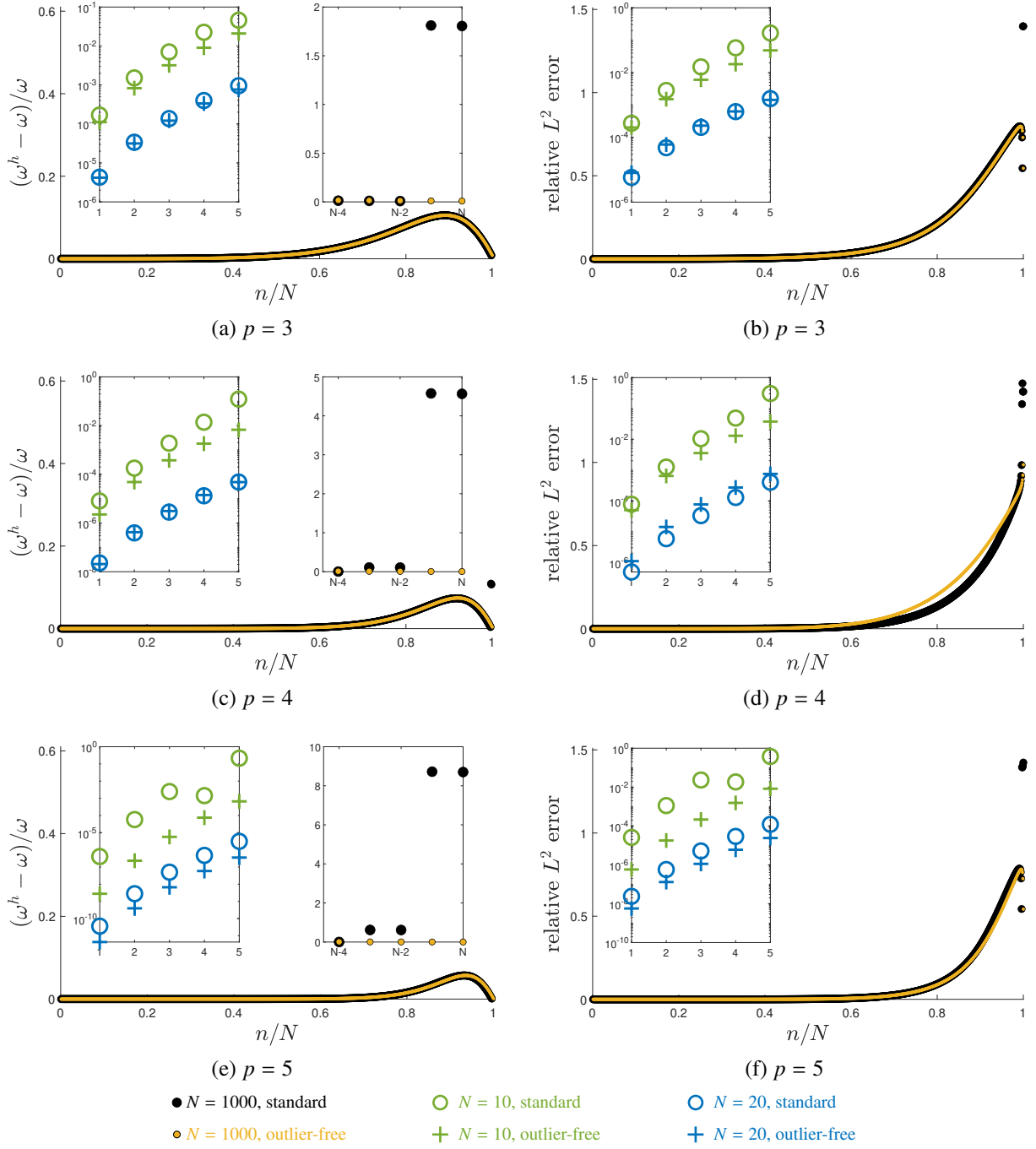


Figure 12: **Normalized frequency error (left) and L^2 errors in the mode shapes (right) of the free vibration of a beam with free boundary conditions.** The three inset figures show, from left to right, the normalized errors in the first five frequencies, the normalized errors in the last five frequencies, and the relative L^2 errors in the first five modes.

310 7. Multivariate study of spectra and modes

In this section, we present normalized frequency and modal error plots corresponding to multivariate second- and fourth-order eigenvalue problems with a range of common boundary conditions, illustrating the benefits of outlier removal for multidimensional spline discretizations.

7.1. Presentation of the data

315 The figures on the following pages present normalized frequency and modal errors for two- and three-dimensional second-order as well as two-dimensional fourth-order eigenvalue problems. To our knowledge, this is the first time that for multidimensional spline discretizations, discrete spectra and modes are correctly identified and presented with respect to their corresponding analytical counterparts. For a detailed account on how these results have been computed, we refer interested
320 readers to Appendix D.

We note that in the univariate case, the natural ascending ordering of the analytical frequencies leads to a smooth representation of the frequency and modal data. In the multivariate setting, however, the situation is more complicated. We have therefore chosen a different ordering that leads to an improved representation of the errors:

- 325 • The frequencies are ordered in such a way that their *normalized frequency error* (6a) is ascending.
- The mode shapes are ordered in such a way that their *relative error in the L^2 norm* (6b) is ascending.

Hence, the frequencies and modal errors are ordered in different ways.

330 Figures 13, 15, 17, 19, 21, 23, and 25 depict normalized spectra, and Figures 14, 16, 18, 20, 22, 24, and 26 plot the relative L^2 errors of the mode shapes. These figures contain multiple layers of information. We point the reader to the most important features:

- 335 • The left columns denote results obtained with B-splines, while the right columns denote results obtained with the outlier-free spline basis. The total number of degrees of freedom N is kept the same in both cases.
- Each row corresponds to results obtained with a fixed polynomial degree, ranging from $p = 3$ to $p = 5$ for fixed boundary conditions, and $p = 2$ to $p = 4$ for free boundary conditions.
- 340 • Each color refers to a particular mesh resolution N (the legend is placed above the caption). In particular, the results in black are run on a very fine mesh and serve as reference values. The reference curves are plotted in the left as well as the right column, allowing direct comparison between B-splines and the outlier-free basis.
- The inset figure in the left column focuses on the outlier frequencies that are present in the upper second half of the spectra obtained with B-splines.

- The inset figure in the right column focuses on the accuracy in the first five frequencies and modes. The results denoted with the symbol “o” are obtained with B-splines and serve as the reference values. The results denoted with the “+” symbol refer to those results obtained with the outlier-free basis.

7.2. *Second-order eigenvalue problems*

We observe that outlier removal works particularly well in second-order problems, irrespective of the dimension or the type of boundary conditions (fixed or free). We summarize our main observations from Figures 13-20. They concisely tell the story:

- All outlier frequencies and modes are successfully removed.
- The accuracy with respect to the reference is maintained over the full range of frequencies and modes, respectively.
- The results obtained with the outlier-free basis are generally more accurate than the results obtained with B-splines, in particular on coarse meshes
- The relative accuracy of the outlier-free basis on coarse meshes is similar as the reference results (black curve) obtained on a fine mesh. On the other hand, the results obtained with B-splines show signs of pre-asymptotic behavior.

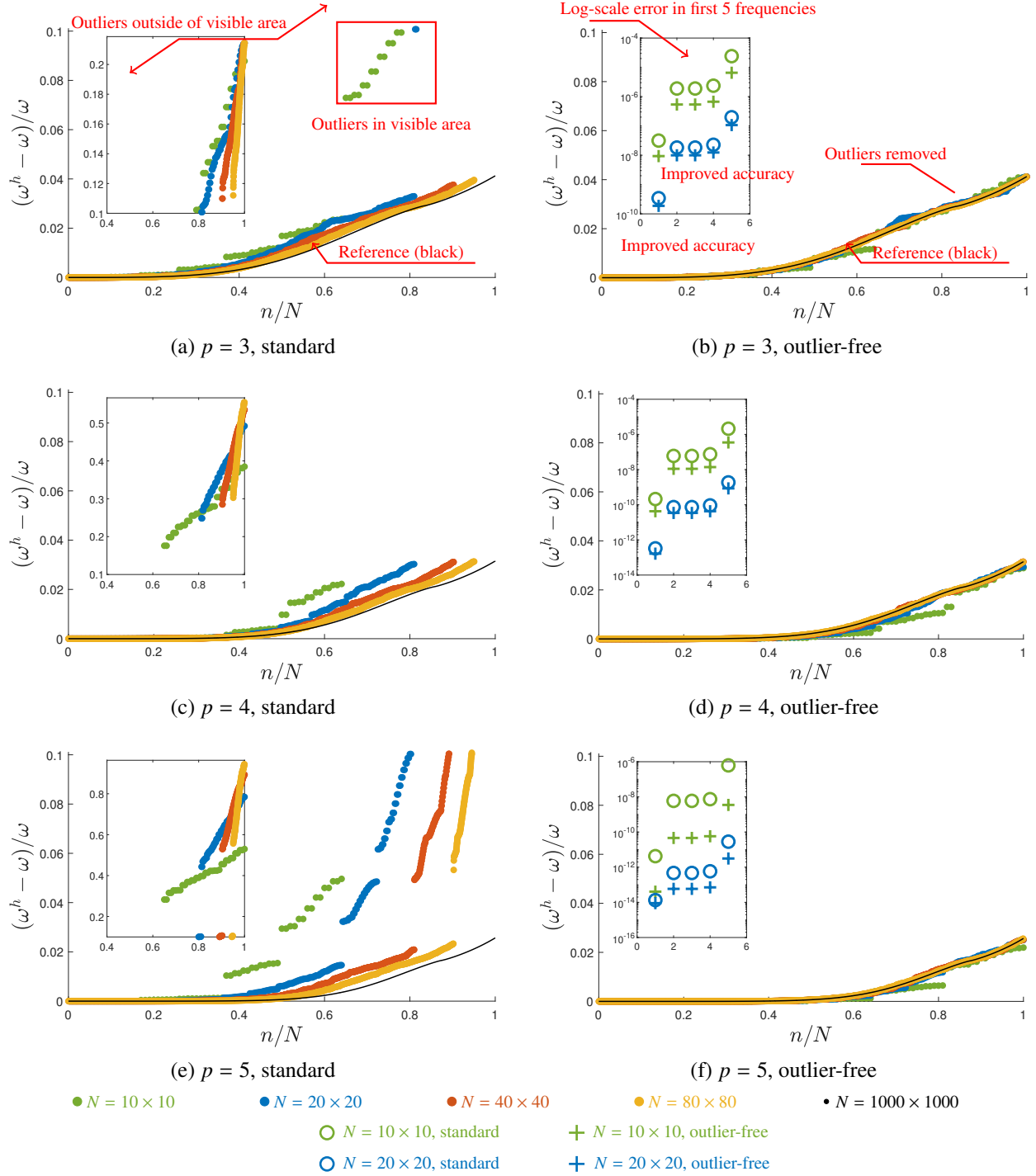


Figure 13: **Normalized frequency error** of the free vibration of a **membrane with fixed boundary conditions**. The left column reports the results obtained with B-splines and the right column reports the results obtained with the outlier-free basis. Note specifically the effect of mesh refinement.

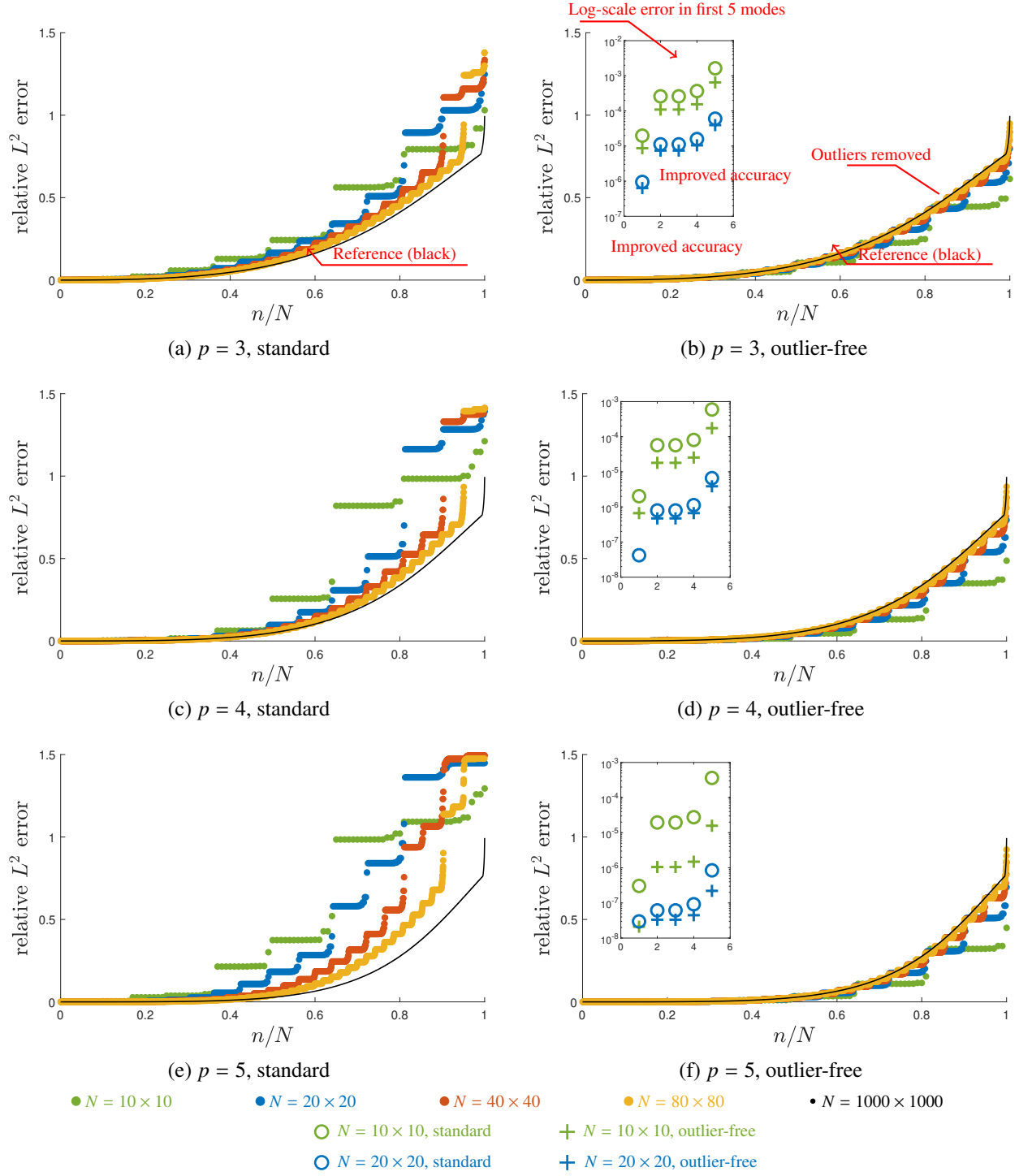
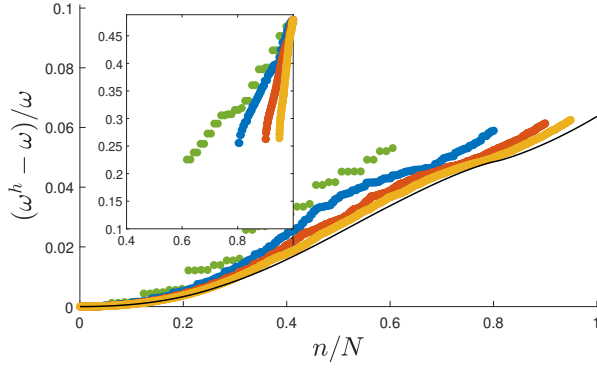
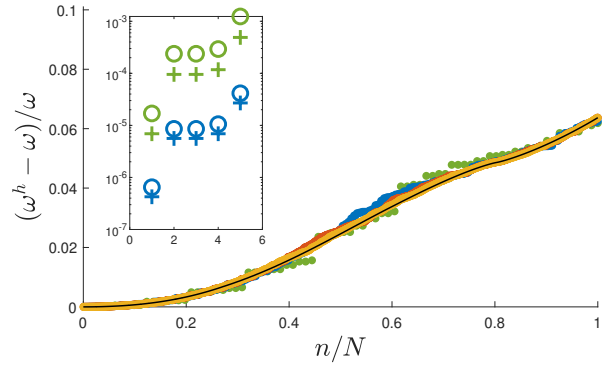


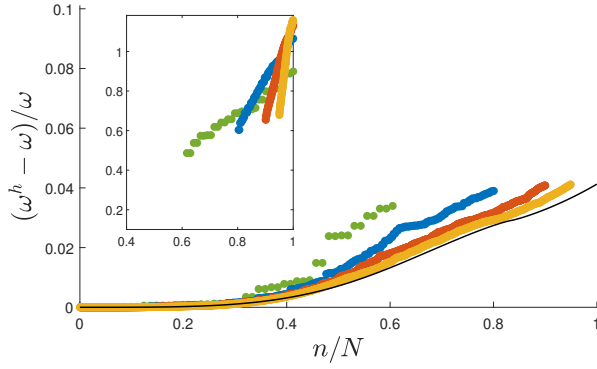
Figure 14: L^2 error in the mode shapes of the free vibration of a membrane with fixed boundary conditions. The left column reports the results obtained with B-splines and the right column reports the results obtained with the outlier-free basis. Note specifically the effect of mesh refinement.



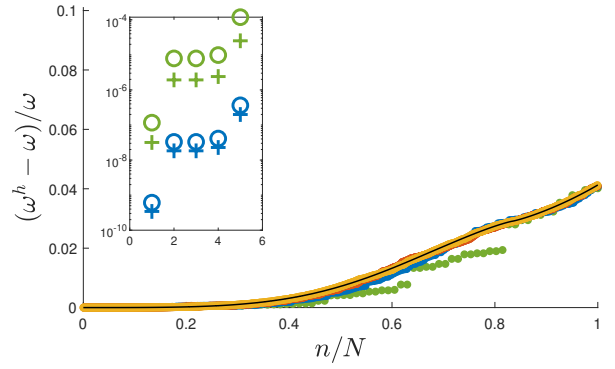
(a) $p = 2$, standard



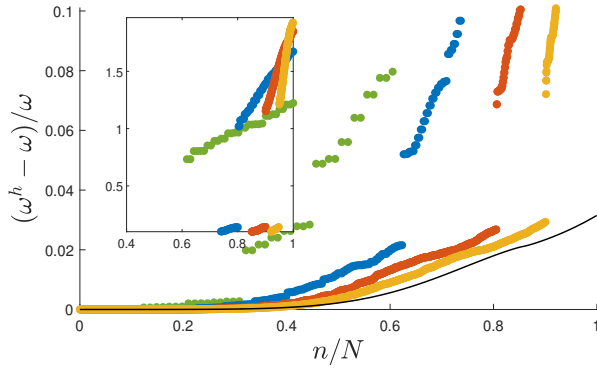
(b) $p = 2$, outlier-free



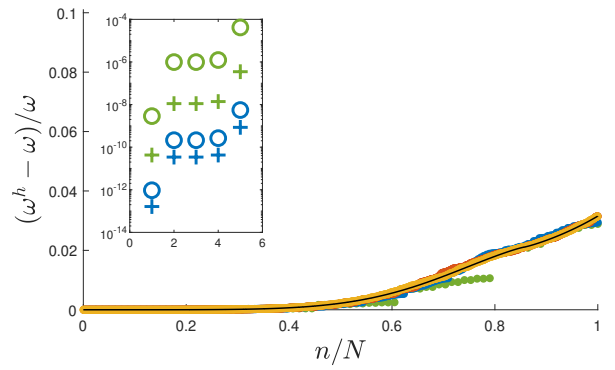
(c) $p = 3$, standard



(d) $p = 3$, outlier-free



(e) $p = 4$, standard



(f) $p = 4$, outlier-free

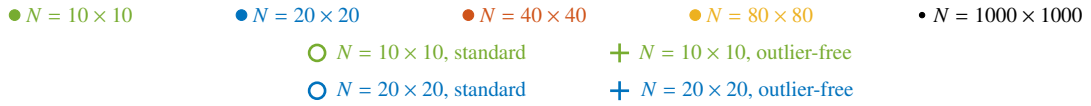
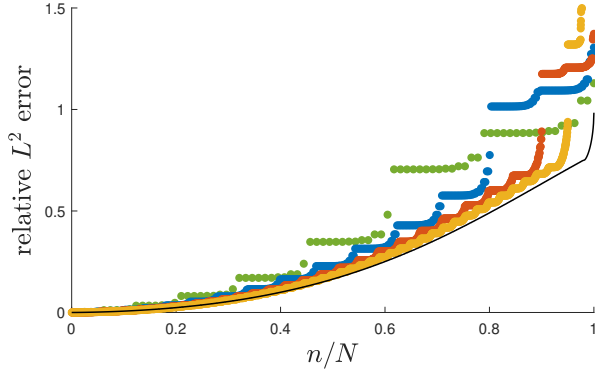
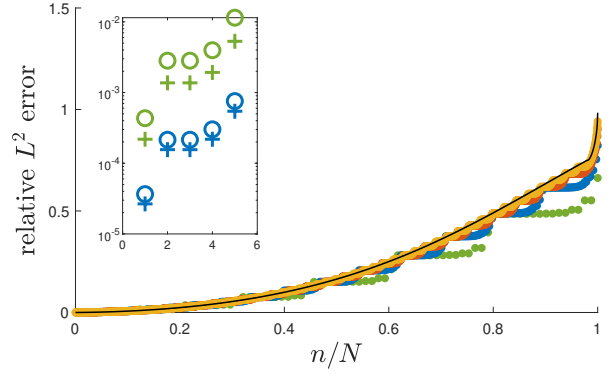


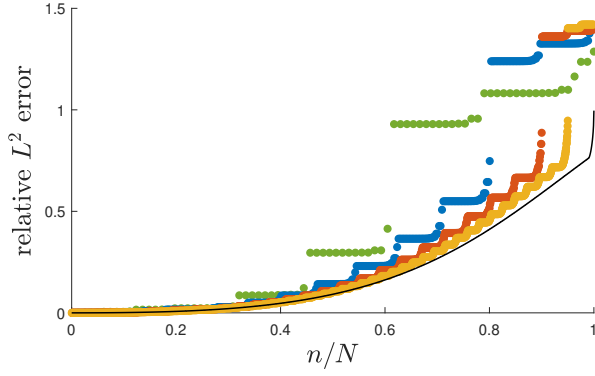
Figure 15: **Normalized frequency error of the free vibration of a membrane with free boundary conditions.** The left column reports the results obtained with B-splines and the right column reports the results obtained with the outlier-free basis. Note specifically the effect of mesh refinement.



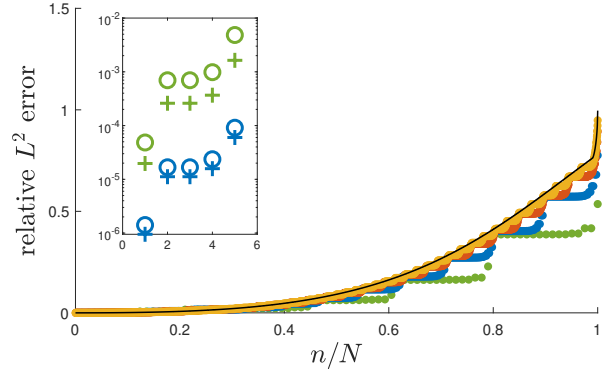
(a) $p = 2$, standard



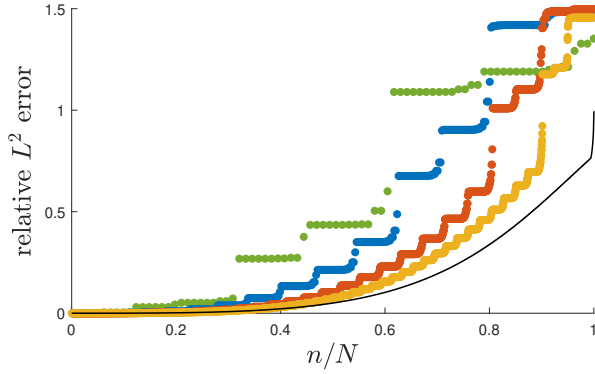
(b) $p = 2$, outlier-free



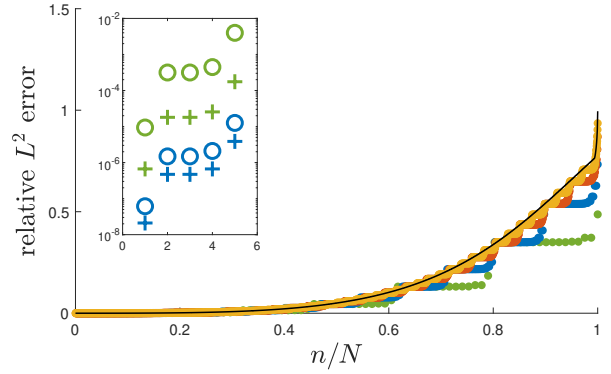
(c) $p = 3$, standard



(d) $p = 3$, outlier-free



(e) $p = 4$, standard



(f) $p = 4$, outlier-free

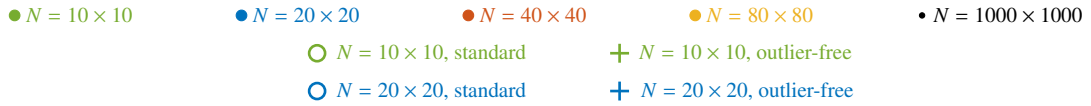
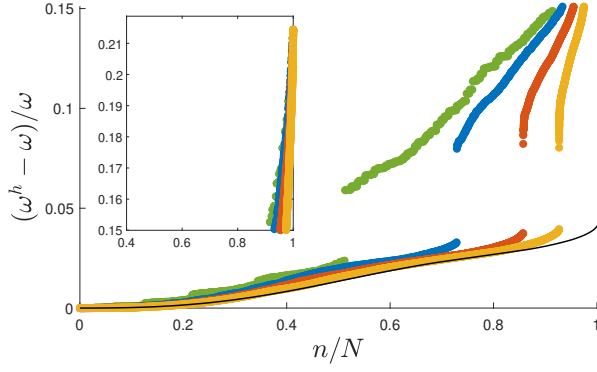
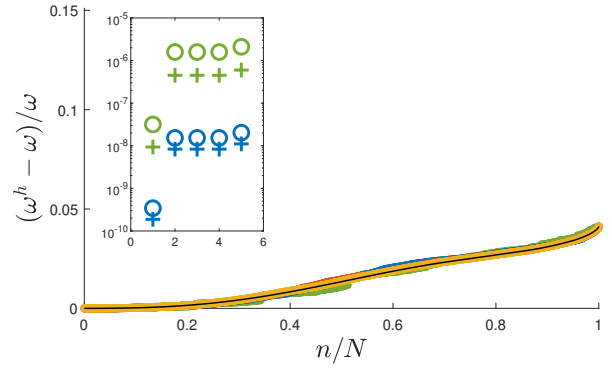


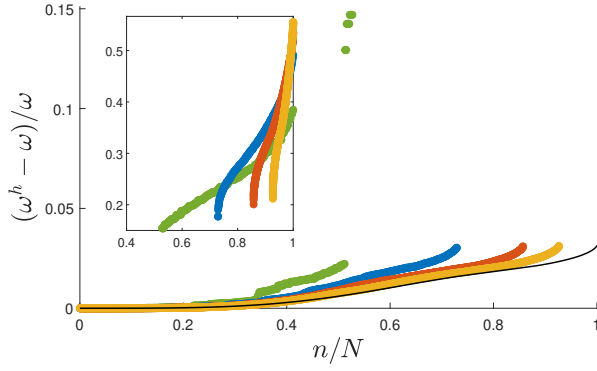
Figure 16: L^2 error in the mode shapes of the free vibration of a membrane with free boundary conditions. The left column reports the results obtained with B-splines and the right column reports the results obtained with the outlier-free basis. Note specifically the effect of mesh refinement.



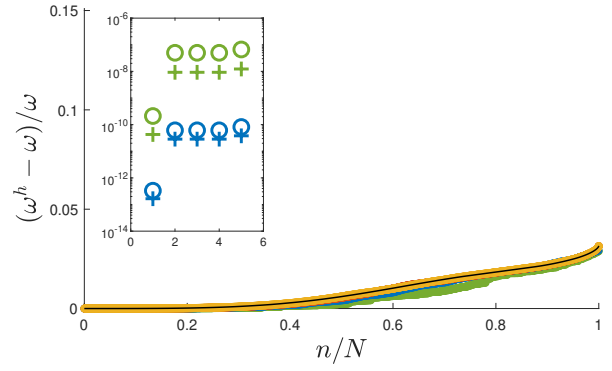
(a) $p = 3$, standard



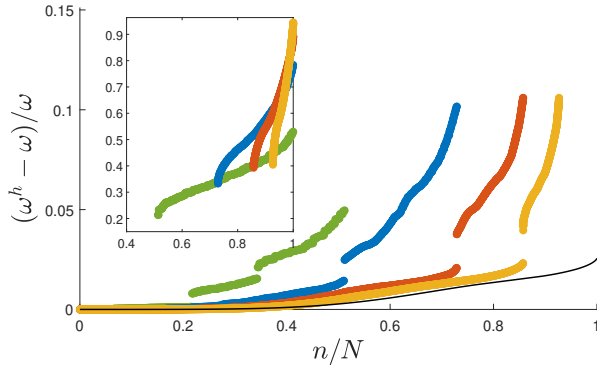
(b) $p = 3$, outlier-free



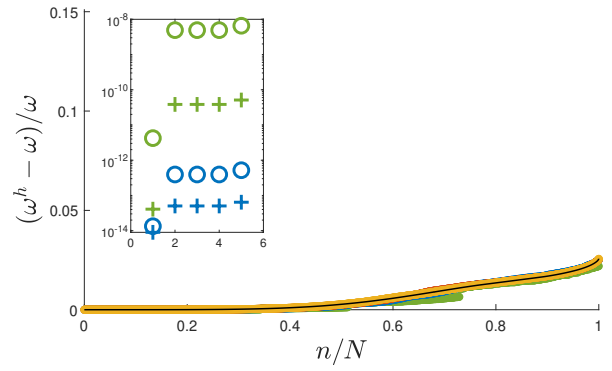
(c) $p = 4$, standard



(d) $p = 4$, outlier-free



(e) $p = 5$, standard



(f) $p = 5$, outlier-free

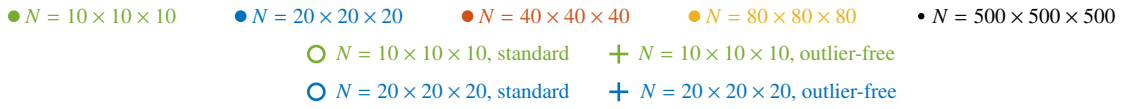
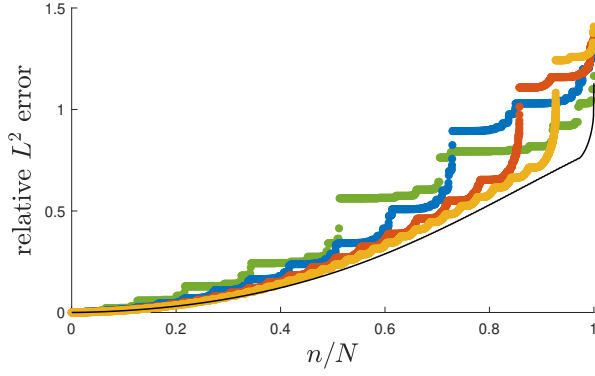
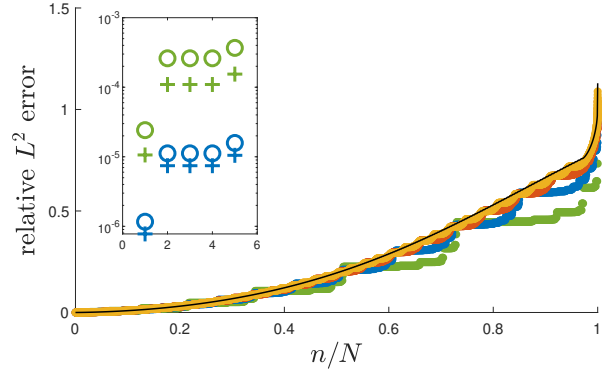


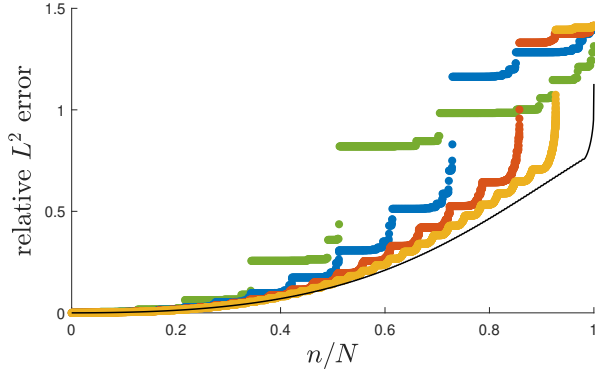
Figure 17: **Normalized frequency error** of the free vibration of a **brick with fixed boundary conditions**. The left column reports the results obtained with B-splines and the right column reports the results obtained with the outlier-free basis. Note specifically the effect of mesh refinement.



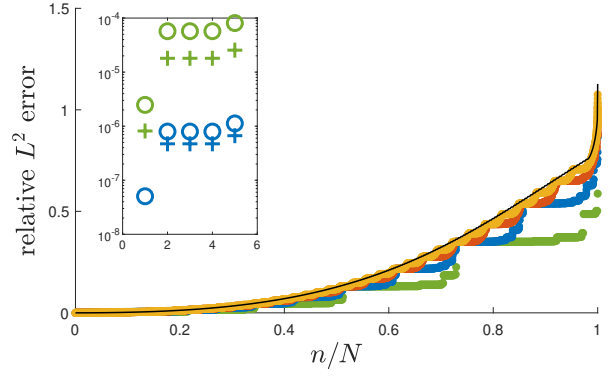
(a) $p = 3$, standard



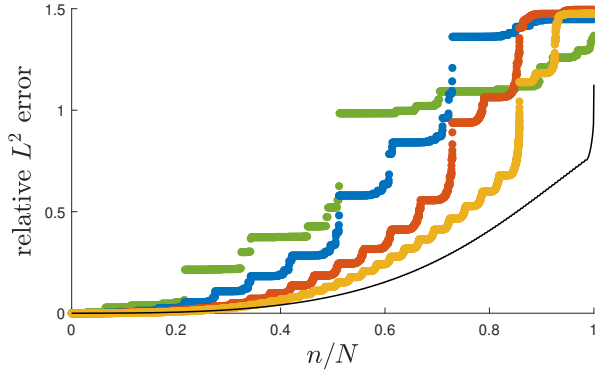
(b) $p = 3$, outlier-free



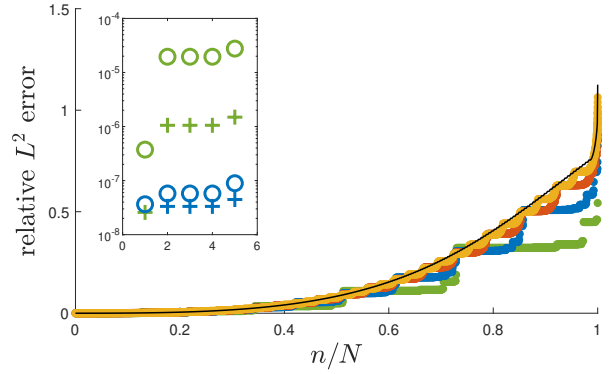
(c) $p = 4$, standard



(d) $p = 4$, outlier-free



(e) $p = 5$, standard



(f) $p = 5$, outlier-free

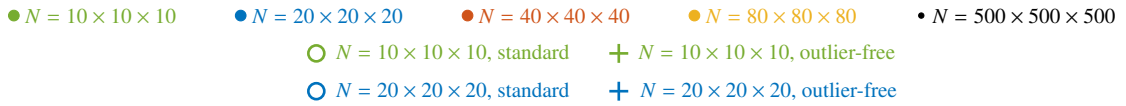
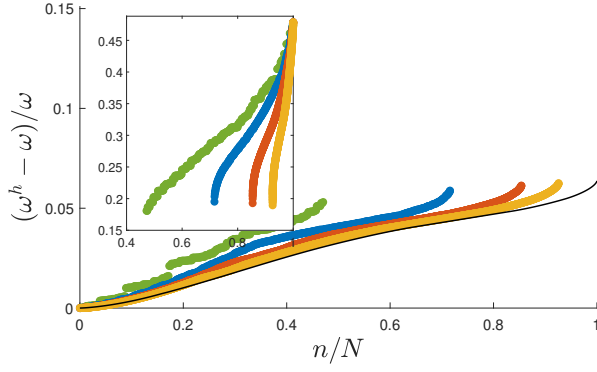
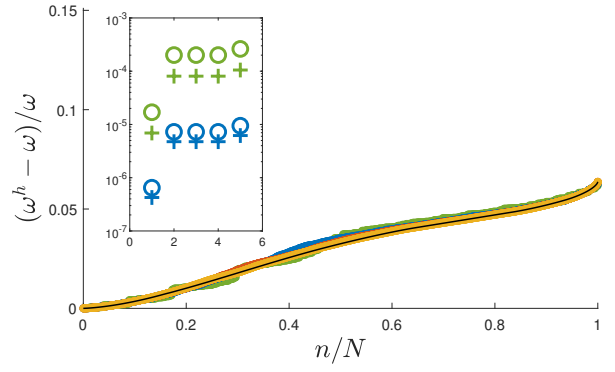


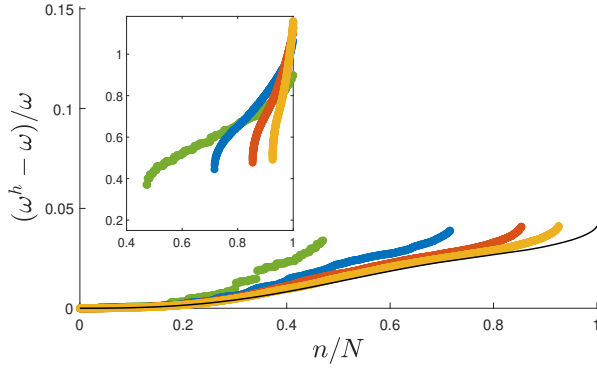
Figure 18: L^2 error in the mode shapes of the free vibration of a brick with fixed boundary conditions. The left column reports the results obtained with B-splines and the right column reports the results obtained with the outlier-free basis. Note specifically the effect of mesh refinement.



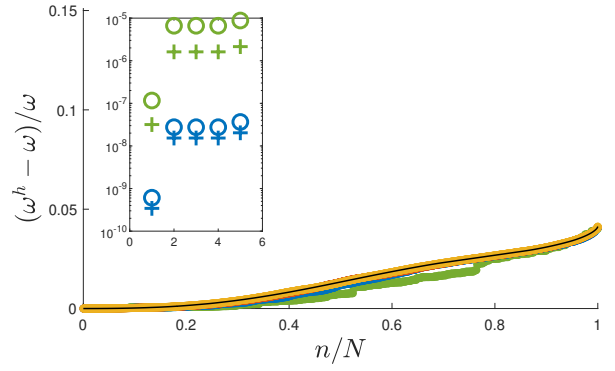
(a) $p = 2$, standard



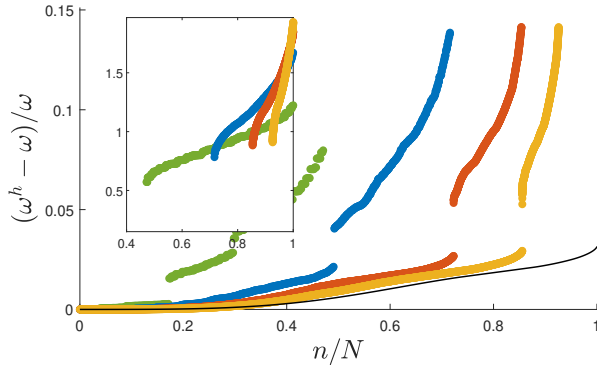
(b) $p = 2$, outlier-free



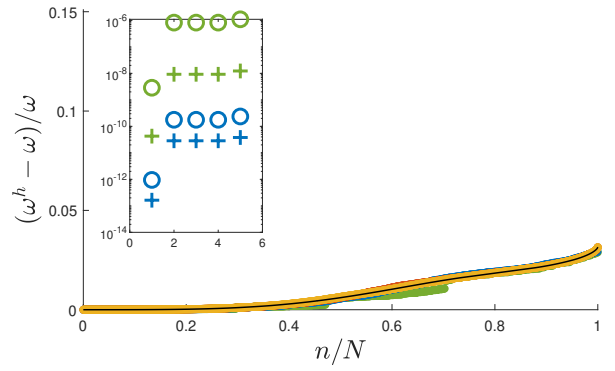
(c) $p = 3$, standard



(d) $p = 3$, outlier-free



(e) $p = 4$, standard



(f) $p = 4$, outlier-free

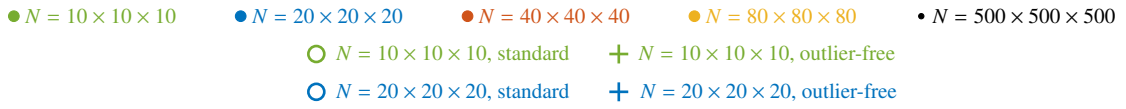
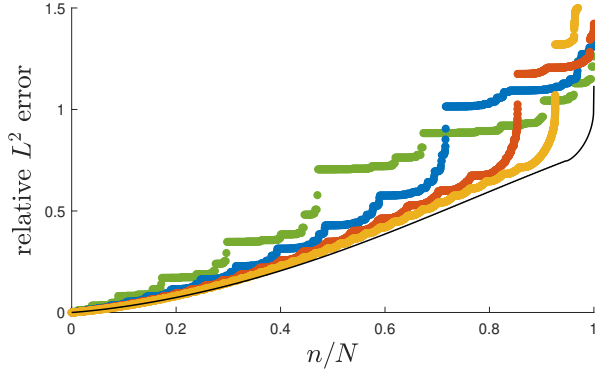
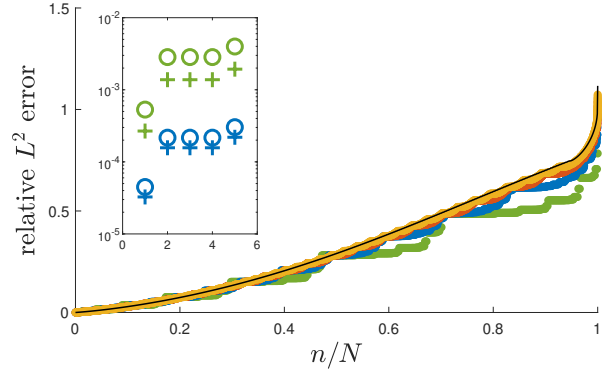


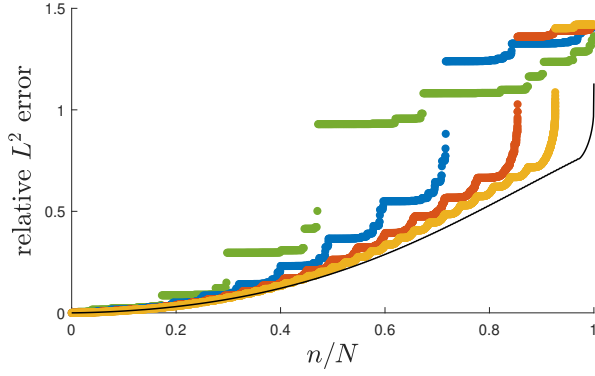
Figure 19: **Normalized frequency error** of the free vibration of a **brick with free boundary conditions**. The left column reports the results obtained with B-splines and the right column reports the results obtained with the outlier-free basis. Note specifically the effect of mesh refinement.



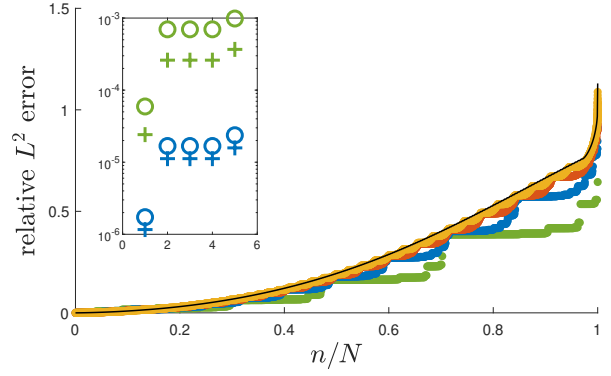
(a) $p = 2$, standard



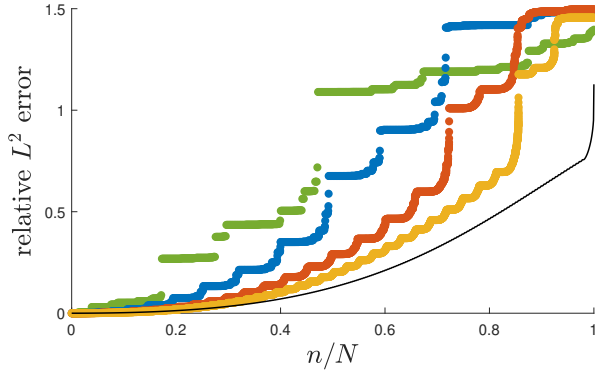
(b) $p = 2$, outlier-free



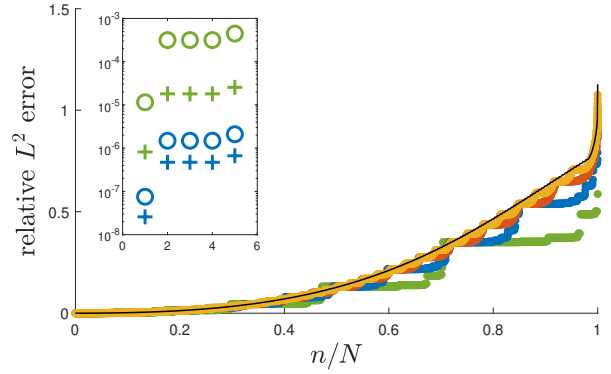
(c) $p = 3$, standard



(d) $p = 3$, outlier-free



(e) $p = 4$, standard



(f) $p = 4$, outlier-free

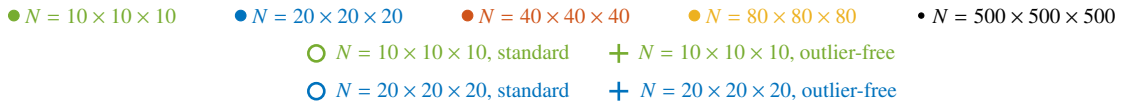


Figure 20: L^2 error in the mode shapes of the free vibration of a brick with free boundary conditions. The left column reports the results obtained with B-splines and the right column reports the results obtained with the outlier-free basis. Note specifically the effect of mesh refinement.

7.3. Fourth-order eigenvalue problems

365 We obtain very promising results for fourth-order problems as well. Overall, the same conclusions may be drawn: outlier frequencies and outlier modes are successfully removed without negatively affecting accuracy in the remaining spectrum. Very good, if not better spectral accuracy is attained over the full range of frequencies and modes. There is one particular observation that we can make for fourth-order problems that we cannot make for second-order problems. Odd degree outlier-free bases seem to perform better than even degrees, particularly on coarse meshes. At this point, we do not know why this happens.

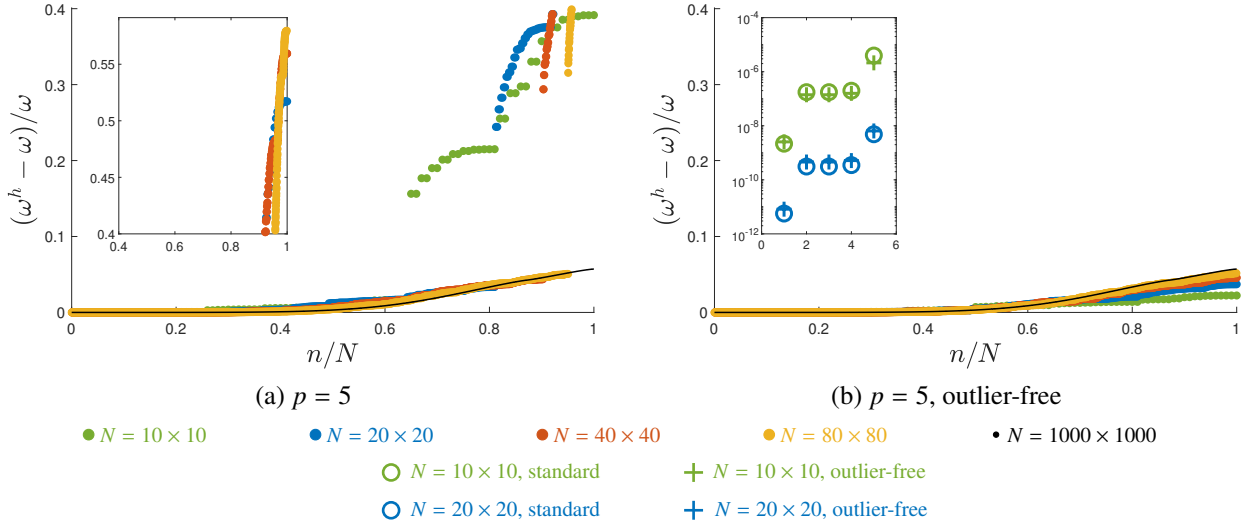


Figure 21: **Normalized frequency error** of the free transverse vibration of a “plate” with fixed boundary conditions. The left column reports the results obtained with B-splines and the right column reports the results obtained with the outlier-free basis. Note specifically the effect of mesh refinement.

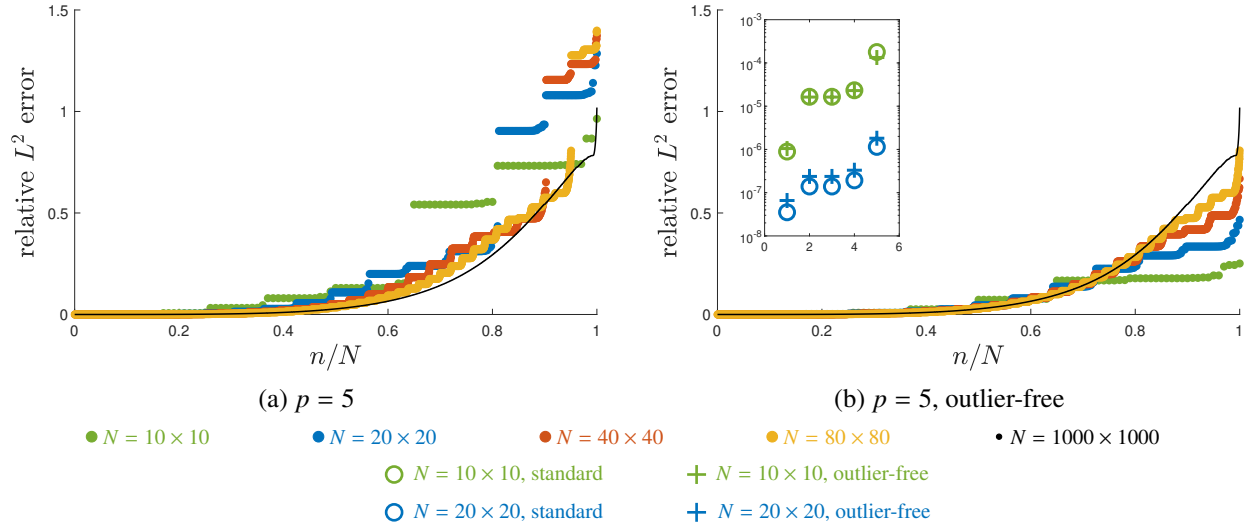
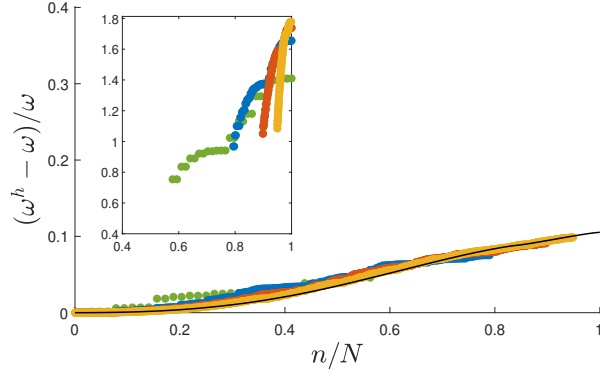
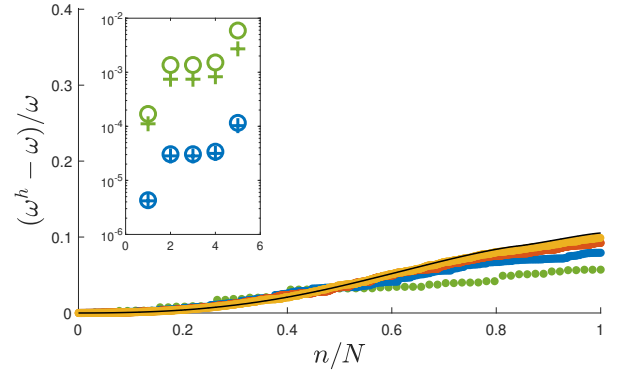


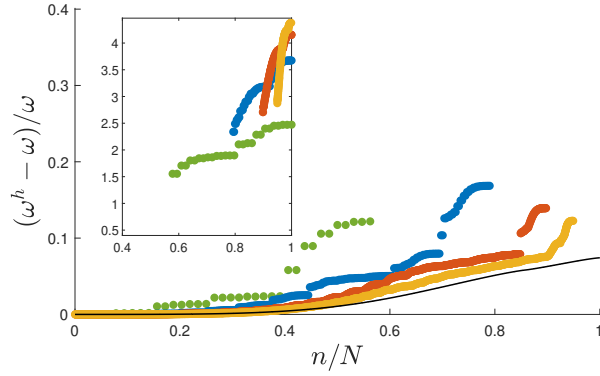
Figure 22: L^2 error in the mode shapes of the free transverse vibration of a “plate” with fixed boundary conditions. The left column reports the results obtained with B-splines and the right column reports the results obtained with the outlier-free basis. Note specifically the effect of mesh refinement.



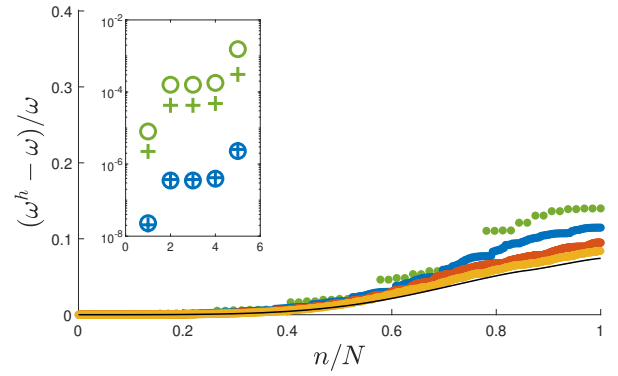
(a) $p = 3$



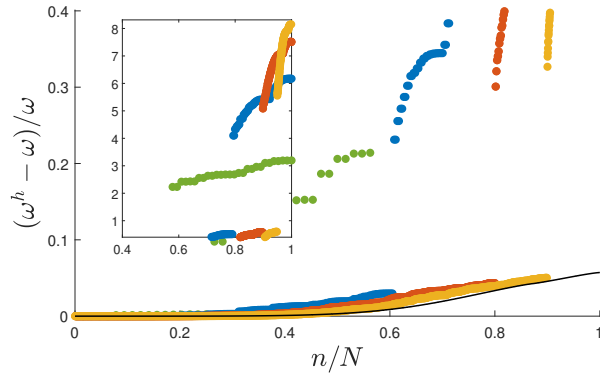
(b) $p = 3$, outlier-free



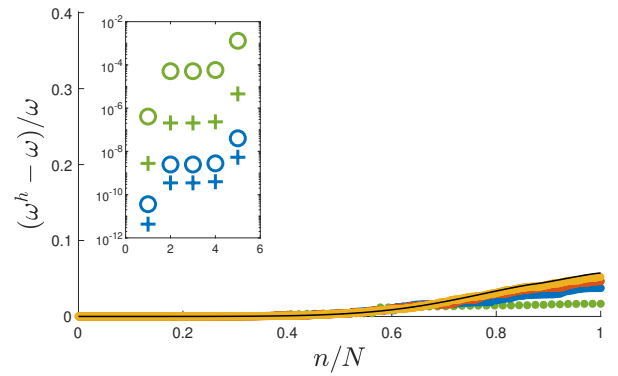
(c) $p = 4$



(d) $p = 4$, outlier-free



(e) $p = 5$



(f) $p = 5$, outlier-free

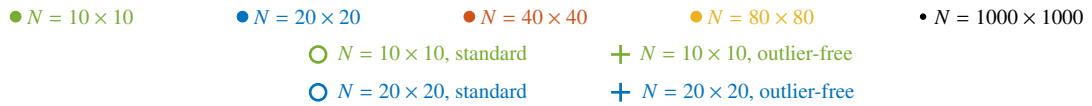


Figure 23: **Normalized frequency error** of the free transverse vibration of a “plate” with simply supported boundary conditions. The left column reports the results obtained with B-splines and the right column reports the results obtained with the outlier-free basis. Note specifically the effect of mesh refinement.

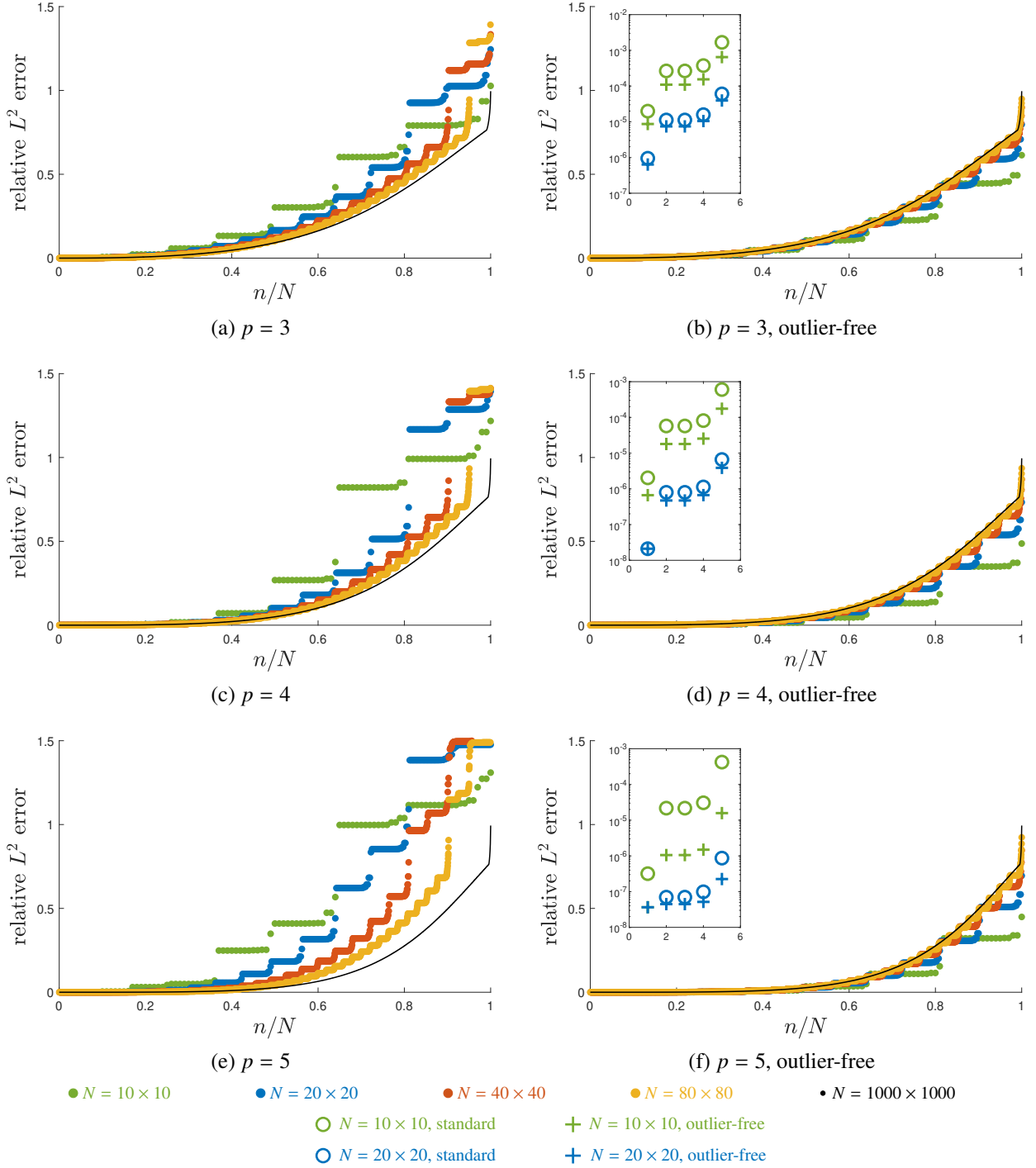


Figure 24: L^2 error in the mode shapes of the free transverse vibration of a “plate” with simply supported boundary conditions. The left column reports the results obtained with B-splines and the right column reports the results obtained with the outlier-free basis. Note specifically the effect of mesh refinement.

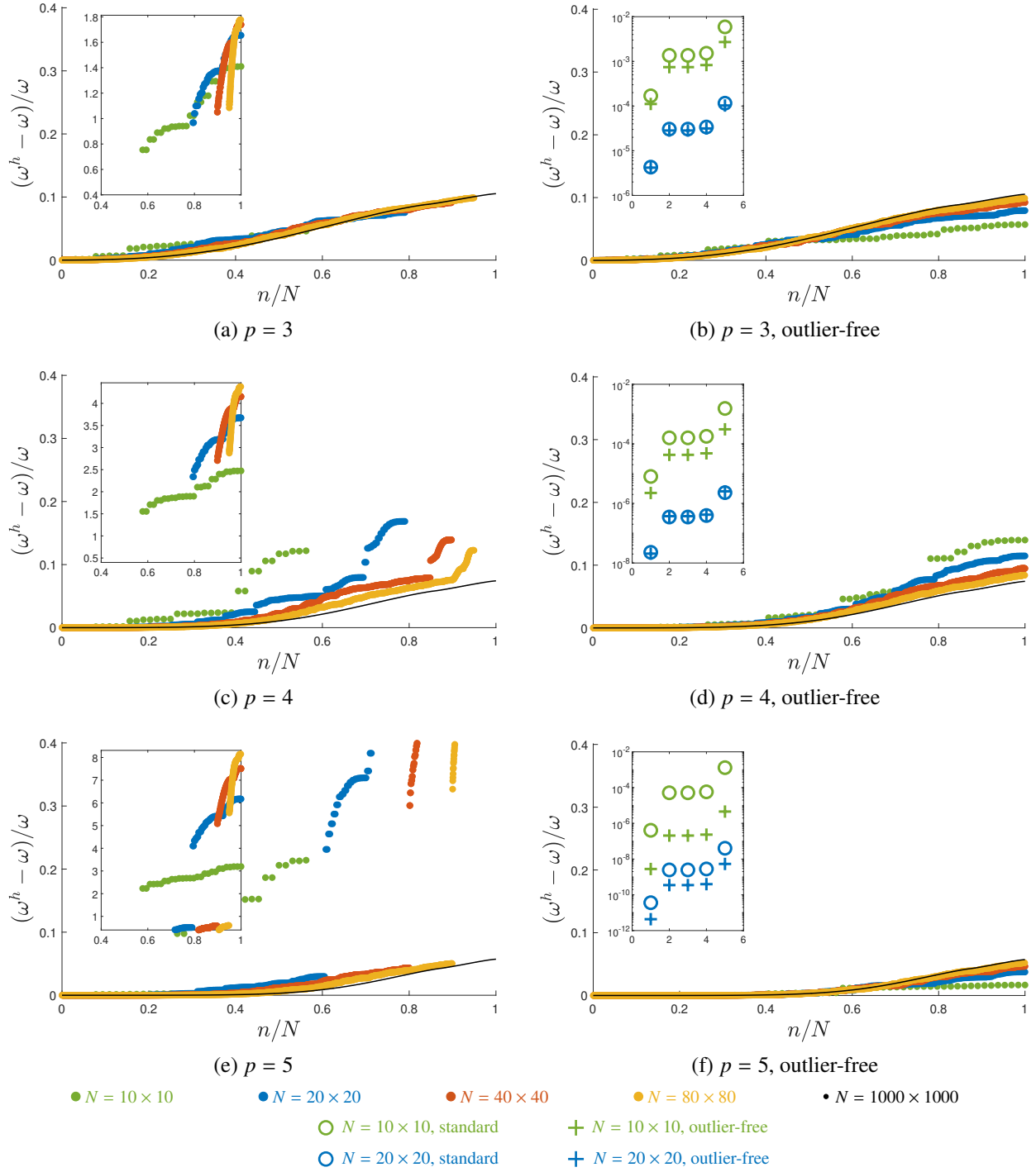


Figure 25: **Normalized frequency error** of the free transverse vibration of a “plate” with free boundary conditions. The left column reports the results obtained with B-splines and the right column reports the results obtained with the outlier-free basis. Note specifically the effect of mesh refinement.

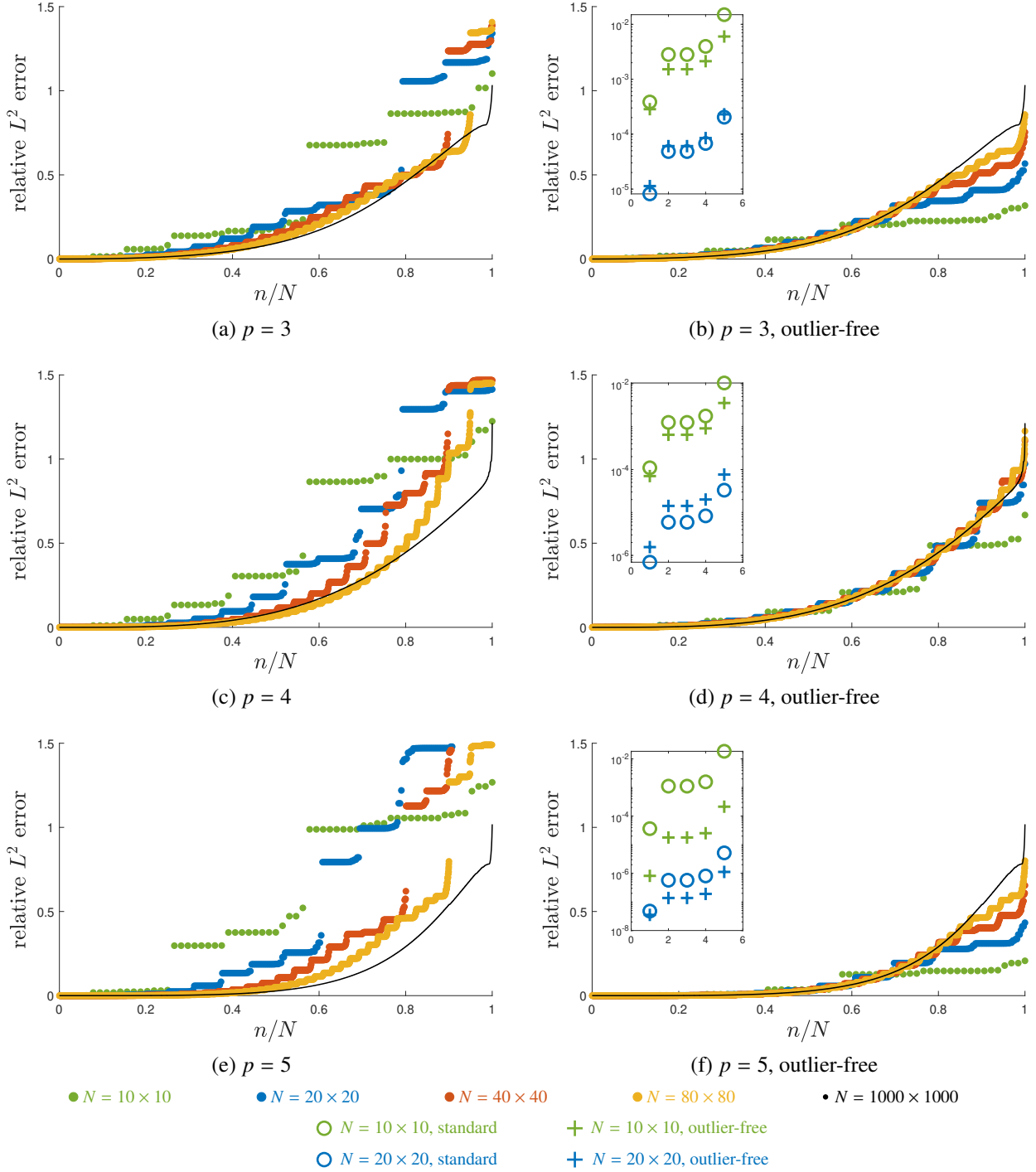


Figure 26: L^2 error in the mode shapes of the free transverse vibration of a “plate” with free boundary conditions. The left column reports the results obtained with B-splines and the right column reports the results obtained with the outlier-free basis. Note specifically the effect of mesh refinement.

8. Application in explicit dynamics

The critical time-step size in explicit dynamics is inversely proportional to the maximum eigenfrequency of the discrete set of equations. Since the outlier frequencies significantly overestimate the true ones, the highest outlier frequency can severely limit the stable time-step size. Hence, successful removal of the outlier modes does not only improve the spatial accuracy of the higher modes, but also prevents the unnecessary decrease of the critical time-step value. In this section, we first verify that outlier removal preserves optimal spatial accuracy in the case of a second order benchmark problem with a non-linear geometry mapping. Thereafter, we investigate how the critical time-step size improves due to outlier removal, as a function of the polynomial degree, the mesh resolution, and the applied boundary conditions. The results depend on the order of the differential operator, but do not depend much on the spatial dimension. Therefore, the study focuses on second- and fourth-order problems, but limits itself to the two-dimensional setting.

8.1. Explicit dynamics of an annular membrane

We consider the free vibration of an annular membrane with inner radius a and outer radius b . The model is fixed at the boundaries. Let $J_4(r)$ denote the 4th Bessel function of the first kind and let λ_k , $k = 1, 2, \dots$ denote its positive zeros. The radii of the annulus are chosen conveniently as certain zeros of $J_4(r)$. In particular $a = \lambda_2 \approx 11.065$ and $b = \lambda_4 \approx 17.616$. As analytical solution we choose the following function, which depends on both the radial coordinate r , the angular coordinate θ , and time t

$$u(r, \theta, t) = J_4(r) \cdot \cos(\lambda_2 t) \cdot \cos(4\theta) \quad (28)$$

It may be verified that the function satisfies the differential equation for free vibration on the annulus with fixed boundary conditions at the inner and outer radii. Figure 27 shows the problem setup, the boundary conditions that are satisfied by u , and its initial condition $u(r, \theta, 0)$.

We compare discretizations obtained with and without outlier removal. Let $\mathbb{S}(0, 2\pi)$ denote a univariate spline space for the angular coordinate, with built-in periodic end-conditions. Furthermore, let $\mathbb{S}^-(a, b)$ and $\mathbb{S}(a, b)$ denote spline spaces for the radial coordinate direction, with and without outlier removal constraints, respectively, see Section 5.5. We consider the multivariate spline spaces

$$\mathbb{S}(a, b) \otimes \mathbb{S}(0, 2\pi) \quad (\text{Standard B-splines}) \quad (29)$$

$$\mathbb{S}^-(a, b) \otimes \mathbb{S}(0, 2\pi) \quad (\text{Outlier-free basis}). \quad (30)$$

The outlier-free basis incorporates two additional boundary constraints for polynomial degrees three and four, and four additional constraints for polynomial degree five.

We perform explicit dynamics with the consistent mass matrix and simulate one full period of the periodic function $u(r, \theta, t)$. In other words, the final time is $T = 2\pi/\lambda_2$. We use polynomial degrees $p = 3, 4, 5$ in combination with uniform refinement resulting in meshes with $n_{\text{elem}} = (8, 16, 32)$ elements in the radial coordinate and $2n_{\text{elem}} = (16, 32, 64)$ elements in the angular coordinate.

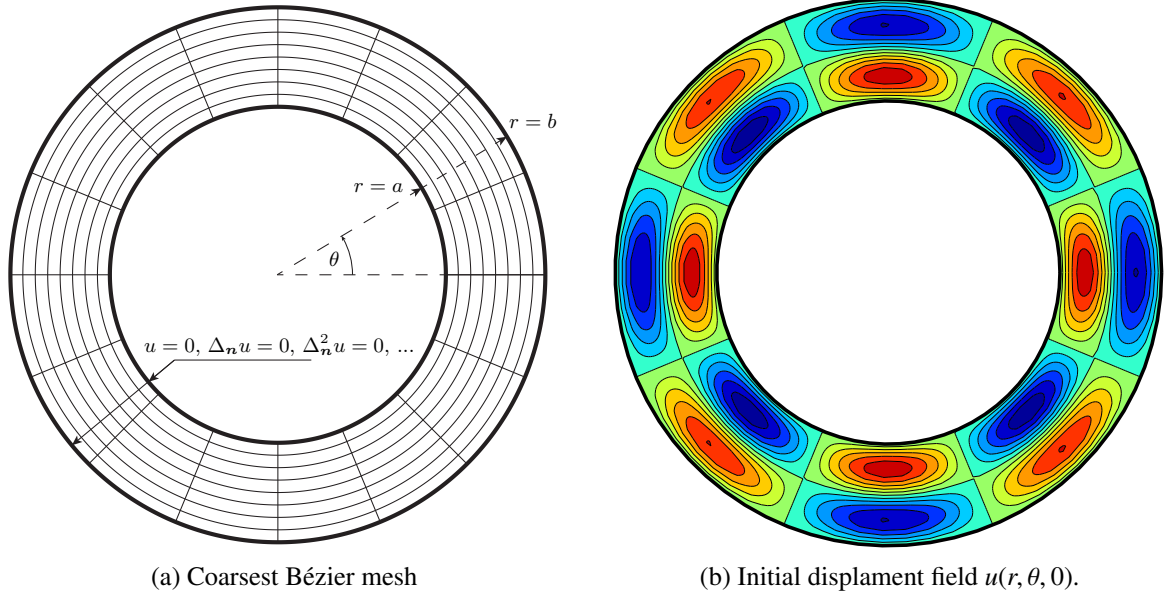


Figure 27: Problem description for explicit dynamics on an annulus.

We choose a very small, order dependent time-step, $\Delta t = (p/(2n_{\text{elem}}))^p$, to verify that spatial accuracy is maintained. The convergence behavior with outlier-free basis is compared with the standard approach in Figure 28. The results are compared as a function of the square root of the total number of degrees of freedom. The outlier-free basis preserves optimal accuracy of the standard approach, however, using fewer degrees of freedom. Improved accuracy is observed, particularly on coarse meshes.

395

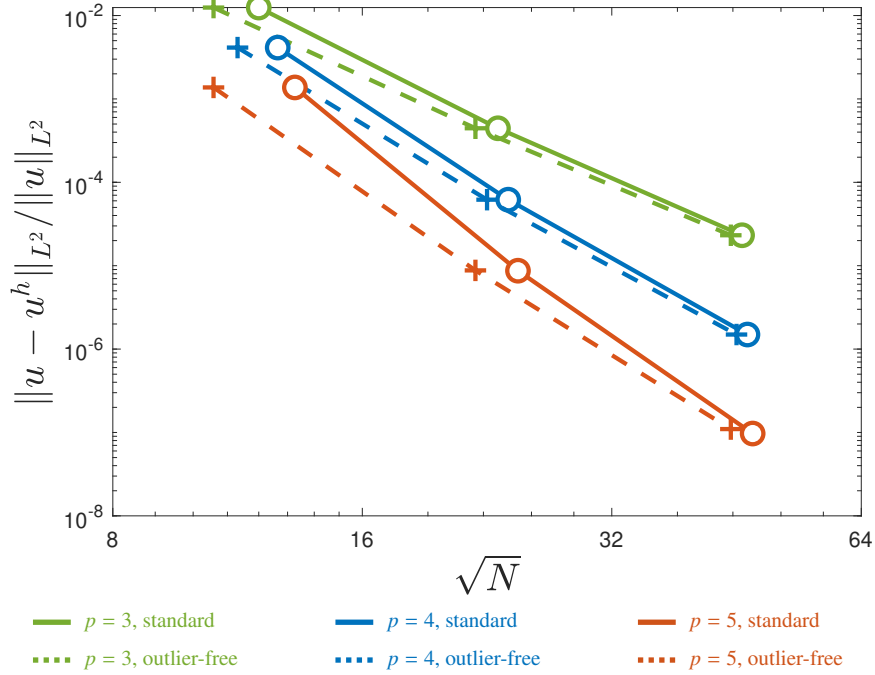


Figure 28: Relative L^2 error in the vertical displacement field u as a function of the square root of number of degrees of freedom N . Due to the additional boundary constraints, the results with outlier removal achieve the same accuracy as the standard approach, however, with fewer degrees of freedom.

8.2. Study of the critical time-step

We consider the semi-discretization (4), obtained with the Galerkin method and a consistent mass matrix⁴. For time integration, we apply the central difference method, which is a special case of the Newmark family, with parameters $\beta = 0$ and $\gamma = 1/2$ [11]. The Newmark method is conditionally stable for parameter values $\gamma \geq \frac{1}{2}$ and $\beta < \frac{\gamma}{2}$, see [11, Chapter 9, Section 1.2, page 492]. For undamped systems, the conditional stability is governed by

$$\omega^h \Delta t \leq \Omega_{\text{crit}}, \quad \Omega_{\text{crit}} = \left(\frac{\gamma}{2} - \beta \right)^{-\frac{1}{2}} \quad (31)$$

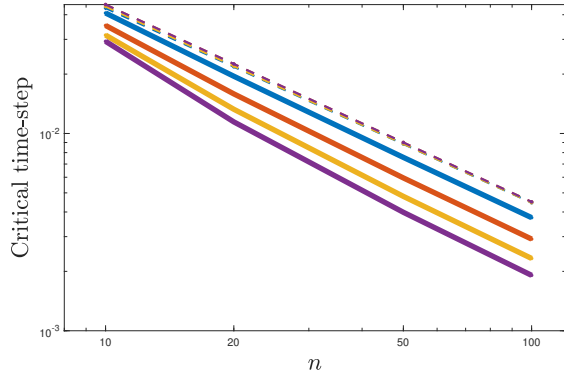
In these cases, the critical time-step size, $\Delta t_{\text{crit}} := \Omega_{\text{crit}} / \omega_{\text{max}}^h$, is inversely proportional to the maximum discrete frequency ω_{max}^h . For example, the central difference method has a critical sampling frequency of $\Omega_{\text{crit}} = 2$, and consequently, the critical time-step size is $\Delta t_{\text{crit}} := 2 / \omega_{\text{max}}^h$.

Figure 29 depicts the absolute value of the critical time step obtained for explicit dynamics of a square membrane, with (a) fixed and (b) free boundary conditions, and explicit dynamics of a square plate, with (c) fixed, (d) simply supported, and (e) fixed boundary conditions. The critical time-step size improves with outlier removal and, importantly, no longer deteriorates with increasing polynomial degree. The relative increase in critical time-step size is plotted in Figure 30.

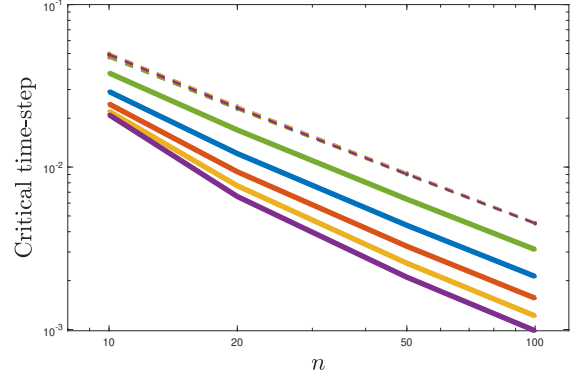
⁴Our approach also works with lumped mass. To show optimal accuracy in space we choose the consistent mass matrix in all our numerical tests, although this is not truly explicit.

Significant advantages can be observed, particularly for higher order discretizations with simply supported and free boundary conditions. Furthermore, we see that fourth-order problems benefit more from outlier removal than second-order problems.

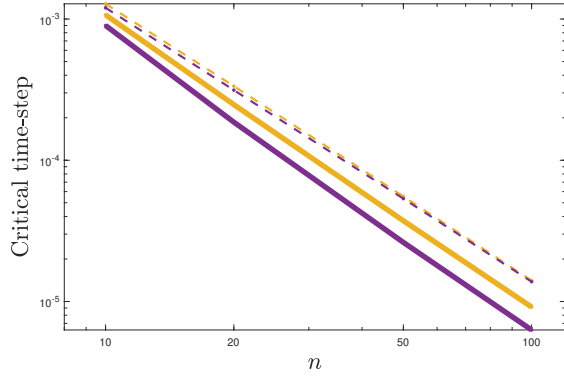
410 **Remark 8.1.** *The results depicted in Figure 30, obtained for explicit dynamics of C^{p-1} discretizations of square membranes and plates, are values that are unlikely to be attained in practical problems. Generally speaking, complex models do not have uniform element sizes and maximum C^{p-1} continuity between all elements. Further investigation is necessary to determine the benefit of outlier removal for industrial-scale problems, which involve multi-patch geometry, and, possibly,*
 415 *trimmed patches [21].*



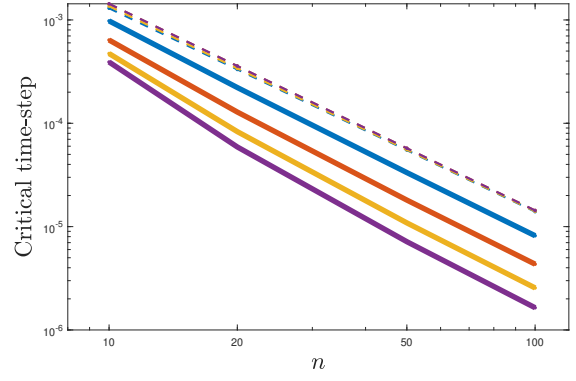
(a) Membrane, fixed bc's



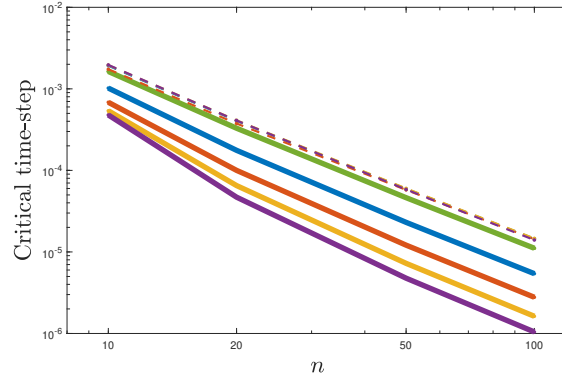
(b) Membrane, free bc's



(c) Plate, fixed bc's



(d) Plate, simply supported bc's



(e) Plate, free bc's

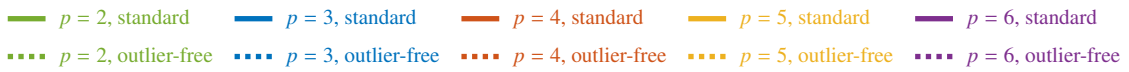
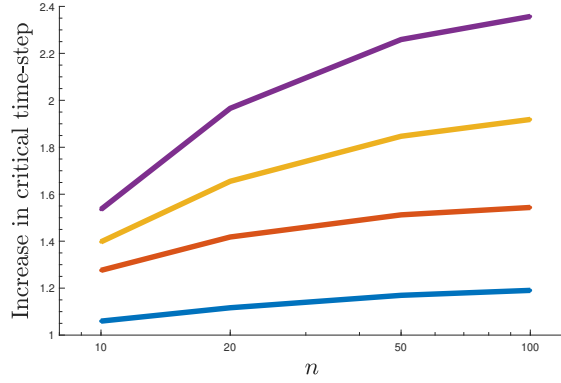
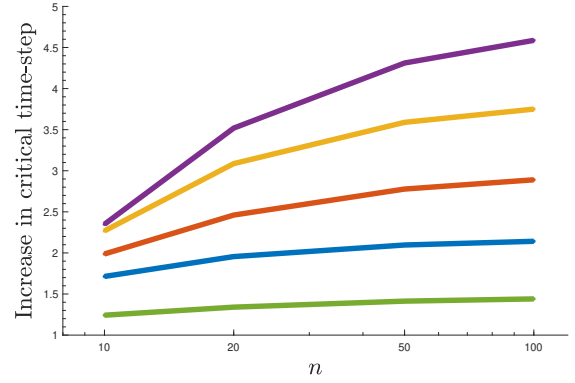


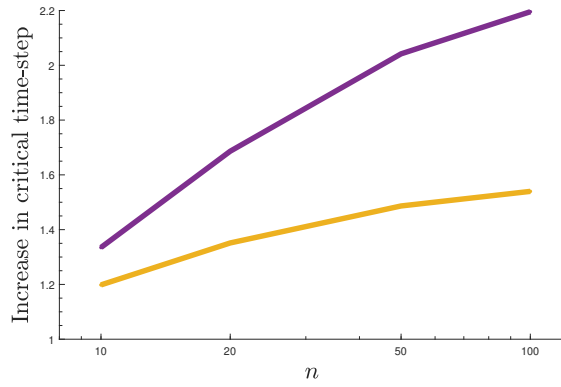
Figure 29: Critical time-step size in explicit dynamics of a square membrane (a,b) and plate (c,d,e), as a function of the mesh resolution $N = n \times n$, with and without outlier removal.



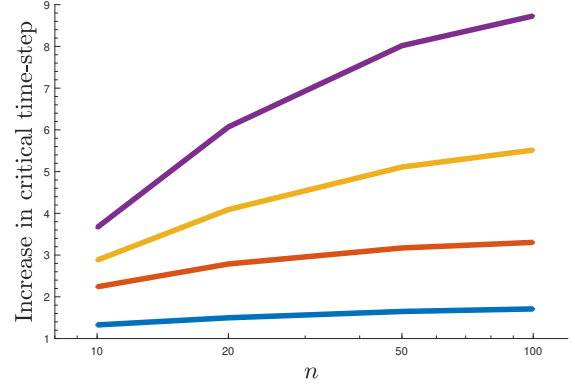
(a) Membrane, fixed bc's



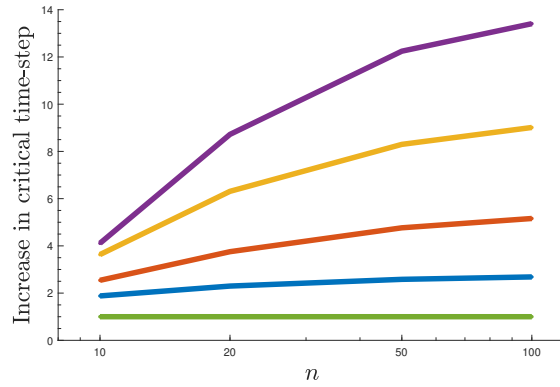
(b) Membrane, free bc's



(c) Plate, fixed bc's



(d) Plate, simply supported bc's



(e) Plate, free bc's

— $p = 2$ — $p = 3$ — $p = 4$ — $p = 5$ — $p = 6$

Figure 30: Increase of the critical time-step size due to outlier removal in explicit dynamics of a square membrane (a,b) and plate (c,d,e), as a function of the mesh resolution $N = n \times n$, with and without outlier removal.

9. Conclusion

In this paper, we studied outlier frequencies and modes in univariate and multidimensional spline discretizations. In particular, we provided a complete characterization for second- and fourth-order problems that involve all common sets of homogeneous boundary conditions. We introduced a new technique that removes outliers without affecting the spectral accuracy in the remainder of the frequencies and modes. The fundamental notion that underlies our approach is that the analytical solution to an eigenvalue problem actually satisfies a sequence of eigenvalue problems (involving higher-order self-adjoint operators), thus satisfying additional boundary constraints. We observed that the spurious outliers disappear once these additional boundary constraints are imposed. Because the analytical modes satisfy the additional constraints, the approach is variationally consistent, and no loss in accuracy is observed for frequencies and mode shapes.

We showed how the additional boundary constraints can be encoded in a specialized Bézier extraction operator, providing a basis for the reduced spline trial space. We also devised an algorithm that computes such extraction operators. We demonstrated that numerical spectra of common structural elements improved significantly when outliers were removed, especially in the multidimensional setting. We finally investigated the improvement in terms of the critical time-step size in explicit dynamics calculations of vibrating membranes and plates, made possible by outlier removal. We observed that the gains in terms of the critical time-step size improve with increasing polynomial degree, and are higher for free boundary conditions than for fixed ones. Our results also demonstrate that the potential gains are much higher for fourth-order problems than for second-order problems.

The results presented in this paper provide new insights into the origin of outlier frequencies and modes in spline discretizations, and illustrate the extent to which they pollute spline spectra. It remains to be seen if our approach to remove outliers can be practically used in industrial-scale problems of complex geometry. We anticipate that certain homogeneous constraints, particularly at free boundaries, can be easily adopted. Others, however, may be more troublesome, for instance when boundary conditions change along the edge or face of a spline patch, and thus also require a change in homogeneous constraints. In the setting of forced vibrations, the constraints may no longer be homogeneous, which requires an extension of the approach presented herein. We hope to investigate and further develop our approach in future work, possibly along the lines presented in Appendix B. Another interesting aspect, requiring further study, is the behavior of outlier frequencies in trimmed isogeometric discretizations [22, 23], in particular in the context of explicit dynamics. A recent study indicates that outliers may be less pronounced in this case [21].

Acknowledgments

René R. Hiemstra and Dominik Schillinger acknowledge generous support from the German Research Foundation through the DFG Emmy Noether Award SCH 1249/2-1. Alessandro Reali acknowledges the support from the Italian Ministry of University and Research (MIUR) through the PRIN project XFAST-SIMS (No. 20173C478N).

Algorithm 1 Computation of a basis for the null space of a single vector

```

1: procedure NULLSPACE( $a \in \mathbb{R}^m$ ) ▷
2:    $C \leftarrow$  zero matrix(size:  $m \times (m - 1)$ )
3:    $i \leftarrow 1$ 
4:   save  $\leftarrow 0$ 
5:   for  $j = 1 : m - 1$  do
6:     if  $a_i == 0$  then
7:        $C_{i,i} \leftarrow 1$ 
8:     else
9:       if  $a_{i+1} == 0$  then
10:         $i \leftarrow i + 1$ 
11:         $C_{i,i} \leftarrow 1$ 
12:      else
13:         $C_{i,j} \leftarrow 1 - \text{save}$ 
14:         $C_{i+1,j} \leftarrow -(a_i/a_{i+1}) * C_{i,j}$ 
15:        save  $\leftarrow C_{i+1,j}$ 
16:      end if
17:    end if
18:     $i \leftarrow i + 1$ 
19:  end for
20:  return  $C$ 
21: end procedure

```

Algorithm 2 Computation of a null space basis

```

1: procedure NULLSPACE_BASIS( $A \in \mathbb{R}^{M \times N}$ ) ▷
2:    $C \leftarrow$  identity matrix(size:  $N \times N$ ) ▷ Initialize null-space basis
3:   for  $k = 1 : M$  do ▷ Loop over constraints
4:      $\tilde{C} \leftarrow$  NULLSPACE( $A_{k,:}$ ) ▷ Compute nullspace of  $k$ -th row of  $A$ 
5:      $C \leftarrow C * \tilde{C}$  ▷ update  $C$ 
6:      $A \leftarrow A * \tilde{C}$  ▷ update  $A$ 
7:   end for
8:   return  $C$ 
9: end procedure

```

Appendix A. Outlier-free extraction algorithm

455 Appendix B. Compatibility with boundary forces and moments

The additional boundary constraints in (20) are satisfied by the exact solution for the case of free vibrations in bars and beams with fixed, simply supported, and free boundary conditions, see Tables 1 and 2, as well as any combination thereof. In the case of forced vibrations, however, where forces and moments appear at the boundary, the exact solution may no longer satisfy these homogeneous constraints. In this case, \mathbb{S}^- may lead to sub-optimal approximation of the low modes, simply because not all polynomials of order p are present in the spline space \mathbb{S}^- of order p .

Example Appendix B.1. Consider the following simple static model problem: find $u \in \mathcal{U}$ such that

$$-u_{,xx} = 1, \quad x \in (0, 1) \tag{B.1}$$

subject to $u(0) = u(1) = 0$. The analytical solution to this problem is $u(x) = -\frac{x}{2}(x - 1)$, which is a function that is in the space \mathbb{S} ($p > 1$). Numerical approximation in the discrete space \mathbb{S} with a consistent numerical method such as the Galerkin method will reproduce the exact solution. The

exact solution, however, is not a function in \mathbb{S}^- , since it clearly does not satisfy homogeneous even derivatives at the boundary. We therefore must expect sub-optimal approximation accuracy with at most second-order convergence in the H^1 semi-norm.

One way to deal with this issue is to apply our method only along boundaries that are unloaded.
 470 Another way to prevent the loss of optimal convergence is to modify the problem formulation in a variationally consistent way. A preliminary idea on how this could be achieved for the above example is presented next.

Example Appendix B.2. We decompose the numerical solution as $u^h = v^h + g^h$, where $v^h \in \mathbb{S}^- \subset \mathbb{S}$ satisfies the prescribed higher-order homogeneous even derivatives at the boundary, and $g^h \in \mathbb{S}$ is designed to satisfy the Dirichlet boundary conditions (which are zero in this example) and the applied forces at the boundary, that is,

$$-g^h_{,xx}|_{x=0} = -g^h_{,xx}|_{x=1} = 1.$$

This can be achieved as follows. Assume g^h is of the following form

$$g^h = c_L \cdot g_L(x) + c_R \cdot g_R(x),$$

where $g_L(x), g_R(x) \in \mathbb{S}$ are arbitrary functions that satisfy

$$\begin{aligned} D^{(j)}g_L|_{x=0} &= D^{(j)}g_R|_{x=1} = \delta_{2j} & j &= 0, 1, \dots, p-1 \\ D^{(j)}g_L|_{x=1} &= D^{(j)}g_R|_{x=0} = 0 & j &= 0, 1, \dots, p-1 \end{aligned}$$

These functions can be easily determined as a linear combination of B-splines, see Figure B.31. In the case that $g^h = -g_L(x) - g_R(x)$ we have that

$$-v^h_{,xx} = 1 + g^h_{,xx}$$

with $v^h(0) = v^h(1) = 0$ and $v^h_{,xx}(0) = v^h_{,xx}(1) = 0$. The updated right-handside, $1 + g^h_{,xx}$, is now compatible with the additional boundary constraints in the trial space \mathbb{S}^- , which means a consistent
 475 numerical method will reproduce the exact solution $u^h = v^h + g^h = -\frac{x}{2}(x-1)$.

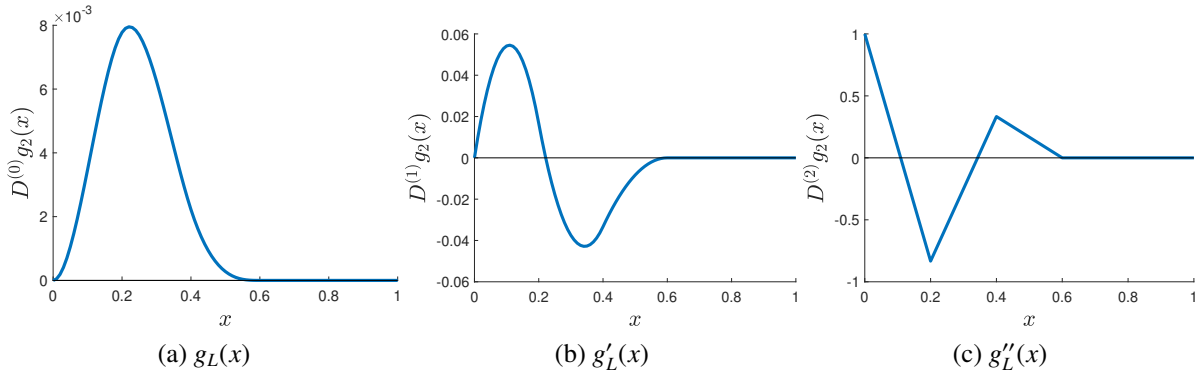


Figure B.31: Cubic boundary functions $g_L(x)$ and their derivatives on a partition (0.0, 0.2, 0.4, 0.6, 0.8, 1.0).

Appendix C. Asymptotic approximation of beam modes

Analytic modes of free vibration of a beam with fixed or free boundary conditions, listed in Table 2, involve hyperbolic sine and cosine functions, which cannot be accurately evaluated beyond mode $n = 10$. In those cases we use the following highly accurate asymptotic approximations

$$W_n(x) = -\exp(-\beta_n x) + (-1)^n \exp(-\beta_n (1-x)) + \cos(\beta_n x) - \sin(\beta_n x) \quad (\text{fixed - fixed}) \quad (\text{C.1a})$$

$$W_n(x) = -\exp(-\beta_n x) + (-1)^n \exp(-\beta_n (1-x)) - \cos(\beta_n x) + \sin(\beta_n x) \quad (\text{free - free}) \quad (\text{C.1b})$$

Appendix D. Computation of multivariate spectra

Practical spectral analysis in the multivariate setting is cumbersome to perform, since the correct identification of discrete and analytical modes is not a trivial task. Furthermore, the computation of all numerical modes on fine meshes becomes computationally intractable due to the curse of dimensionality. In the following, we sketch our approach to circumvent these problems.

Appendix D.1. Correct identification of analytical and numerical eigenmodes

Our approach is motivated by a two-dimensional second-order eigenvalue problem with homogeneous (fixed) boundary conditions. It may be verified that all other cases discussed in this paper allow a similar treatment. In the following we assume basic knowledge of Kronecker matrices and their properties, see [24, Chapter 12, Section 3].

Kronecker product structure of the analytical solution

Consider the second-order eigenvalue problem: find $(U, \lambda) \in \mathcal{V} \times \mathbb{R}^+$ such that

$$\Delta U(x, y) = \lambda U(x, y), \quad (x, y) \in [0, 1]^2. \quad (\text{D.1})$$

If $U \in \mathcal{V}$ has homogeneous boundary conditions, then the eigenvalues and eigenfunctions are

$$\lambda_{kl} = \pi^2(k^2 + l^2), \quad U_{kl}(x, y) = \sin(k \cdot \pi x) \cdot \sin(l \cdot \pi y) \quad (\text{D.2})$$

Due to the Kronecker product structure, the analytical solution can also be factored as follows

$$\lambda_{kl} = \lambda_k + \lambda_l, \quad U_{kl}(x, y) = U_k(x) \cdot U_l(y) \quad (\text{D.3})$$

where $U_k(x) = \sin(k \cdot \pi x)$, $\lambda_k = \pi^2 k^2$ are an eigenpair solution to the univariate eigenvalue problem

$$\Delta U(x) = \lambda U(x), \quad x \in [0, 1]. \quad (\text{D.4})$$

Kronecker product structure of the discrete solution

The discrete solution can be factorized in an analogous form. Consider the generalized eigenvalue problem: find $(\mathbf{u}, \lambda^h) \in \mathbb{R}^N \times \mathbb{R}$ such that

$$\mathbf{K} \mathbf{u} = \lambda^h \mathbf{M} \mathbf{u}. \quad (\text{D.5})$$

Here \mathbf{K} denotes the symmetric semi-definite stiffness matrix and \mathbf{M} the symmetric positive definite mass matrix.

Instead of the generalized eigenvalue problem, it is convenient to consider the standard eigenvalue problem (see [25, Chapter 9, Section 2.2, Page 225]): find $(\mathbf{v}, \lambda^h) \in \mathbb{R}^N \times \mathbb{R}$ such that

$$\tilde{\mathbf{K}} \mathbf{v} = \lambda^h \mathbf{v}. \quad (\text{D.6})$$

with $\tilde{\mathbf{K}} = \mathbf{L}^{-1} \mathbf{K} \mathbf{L}^{-T}$. Here \mathbf{L} denotes the lower triangular matrix in the Cholesky factorization of the mass matrix, $\mathbf{M} = \mathbf{L} \mathbf{L}^T$. The eigenvalues of both problems are the same. The eigenvectors are related according to $\mathbf{u} = \mathbf{L}^{-T} \mathbf{v}$.

We consider the specific case of a tensor-product discretization defined on the unit square $[0, 1]^2$, and assume the same discretization in each coordinate direction. In this case, the mass and stiffness matrices can be factorized in terms of Kronecker products, that is

$$\mathbf{K} = \mathbf{M} \otimes \mathbf{K} + \mathbf{K} \otimes \mathbf{M}, \quad \mathbf{M} = \mathbf{M} \otimes \mathbf{M} \quad (\text{D.7})$$

where \mathbf{K} and \mathbf{M} denote, respectively, the stiffness and mass matrices corresponding to the univariate discretization. Matrix \mathbf{L} also allows a Kronecker product representation, $\mathbf{L} = \mathbf{L} \otimes \mathbf{L}$, where \mathbf{L} is the lower triangular matrix in the Cholesky factorization of the univariate mass matrix, $\mathbf{M} = \mathbf{L} \mathbf{L}^T$. Using the mixed product property of Kronecker product matrices, see [24, Chapter 12, Section 3, Page 707], $\tilde{\mathbf{K}}$ allows the following factorization

$$\tilde{\mathbf{K}} = (\mathbf{L}^{-1} \otimes \mathbf{L}^{-1}) (\mathbf{M} \otimes \mathbf{K} + \mathbf{K} \otimes \mathbf{M}) (\mathbf{L}^{-T} \otimes \mathbf{L}^{-T}) = \mathbf{I} \otimes \tilde{\mathbf{K}} + \tilde{\mathbf{K}} \otimes \mathbf{I}. \quad (\text{D.8})$$

with $\tilde{\mathbf{K}} = \mathbf{L}^{-1} \mathbf{K} \mathbf{L}^{-T}$. Matrix $\tilde{\mathbf{K}}$ is a Kronecker sum matrix, which has the following eigenvalue decomposition (see [26, Chapter 4, Section 4, Page 268])

$$\tilde{\mathbf{K}} = \mathbf{V} \mathbf{\Lambda} \mathbf{V}^T = (\mathbf{V} \otimes \mathbf{V}) (\mathbf{I} \otimes \mathbf{\Lambda} + \mathbf{\Lambda} \otimes \mathbf{I}) (\mathbf{V}^T \otimes \mathbf{V}^T) \quad (\text{D.9})$$

Here, $\tilde{\mathbf{K}} = \mathbf{V} \mathbf{\Lambda} \mathbf{V}^T$ denotes the eigenvalue decomposition of the matrix $\tilde{\mathbf{K}}$. It follows that the eigenvalues and eigenfunctions of the original matrix problem (D.5) are, in matrix notation,

$$\mathbf{\Lambda} = \mathbf{I} \otimes \mathbf{\Lambda} + \mathbf{\Lambda} \otimes \mathbf{I}, \quad \mathbf{U} = \mathbf{L}^{-T} \mathbf{V} = (\mathbf{L}^{-T} \otimes \mathbf{L}^{-T}) (\mathbf{V} \otimes \mathbf{V}) = \mathbf{L}^{-T} \mathbf{V} \otimes \mathbf{L}^{-T} \mathbf{V} = \mathbf{U} \otimes \mathbf{U}. \quad (\text{D.10})$$

Hence, the discrete eigenfrequencies and eigenvectors of the multi-dimensional eigenvalue problem can be represented in terms of discrete eigenfrequencies and eigenvectors of the univariate eigenvalue problem. Let λ_k^h denote the k^{th} eigenvalue in $\mathbf{\Lambda}$ and let $\mathbf{U}_k = \mathbf{L}^{-T} \mathbf{V}_k$ denote its corresponding eigenvector. Furthermore, let $u_k^h(x)$ denote the mode shape obtained by taking the linear combination of the coefficients in \mathbf{U}_k with the basis functions. Then, the numerical eigenvalues and mode shapes of the two-dimensional eigenvalue problem are

$$\lambda_{kl}^h = \lambda_k^h + \lambda_l^h, \quad U_{kl}^h(x, y) = U_k^h(x) \cdot U_l^h(y) \quad (\text{D.11})$$

For fixed k and l , the analytical and numerical frequencies in (D.3) and (D.11), respectively, can be directly compared. Hence, the tensor-product representations enable the correct identification between analytical and numerical modes, which is otherwise cumbersome to achieve.

Appendix D.2. Error analysis of multivariate spectra

Errors in eigenvalues and mode shapes of the two-dimensional eigenvalue problem can be computed in terms of errors in eigenvalues and mode shapes of the corresponding univariate eigenvalue problem. The relative error in the eigenvalue is

$$\frac{\lambda_{kl}^h - \lambda_{kl}^h}{\lambda_{kl}} = \frac{\lambda_k - \lambda_k^h}{\lambda_k + \lambda_l} + \frac{\lambda_l - \lambda_l^h}{\lambda_k + \lambda_l}, \quad (\text{D.12})$$

From linearity and symmetry of the L^2 inner product, the L^2 error in the mode shapes follows as

$$\|U_{kl} - U_{kl}^h\|_{L^2}^2 = (U_{kl} - U_{kl}^h, U_{kl} - U_{kl}^h)_{L^2} = (U_{kl}, U_{kl})_{L^2} - 2(U_{kl}, U_{kl}^h)_{L^2} + (U_{kl}^h, U_{kl}^h)_{L^2} \quad (\text{D.13})$$

For a pair of square integrable functions of the form, $g_1(x) \cdot g_2(y)$ and $h_1(x) \cdot h_2(y)$, defined on $[0, 1]^2$, we have the following identity

$$(g_1 \cdot g_2, h_1 \cdot h_2)_{L^2([0,1]^2)} = (g_1, h_1)_{L^2([0,1])} \cdot (g_2, h_2)_{L^2([0,1])} \quad (\text{D.14})$$

Consequently, the relative L^2 errors in the mode shapes can be computed from the L^2 errors in the univariate mode shapes. We have (suppressing the L^2 spaces involved)

$$\frac{\|U_{kl} - U_{kl}^h\|^2}{\|U_{kl}\|^2} = \frac{\|U_k\|^2 \cdot \|U_l\|^2 - 2(U_k, U_k^h) \cdot (U_l, U_l^h) + \|U_k^h\|^2 \cdot \|U_l^h\|^2}{\|U_k\|^2 \cdot \|U_l\|^2}. \quad (\text{D.15})$$

References

- [1] T. J. R. Hughes, J. A. Cottrell, and Y. Bazilevs. Isogeometric analysis: CAD, finite elements, NURBS, exact geometry and mesh refinement. *Computer Methods in Applied Mechanics and Engineering*, 194(39):4135–4195, October 2005.
- [2] D. J. Benson, Y. Bazilevs, M. C. Hsu, and T. J. R. Hughes. A large deformation, rotation-free, isogeometric shell. *Computer Methods in Applied Mechanics and Engineering*, 200(13):1367–1378, March 2011.
- [3] S. Lipton, J. A. Evans, Y. Bazilevs, T. Elguedj, and T. J. R. Hughes. Robustness of isogeometric structural discretizations under severe mesh distortion. *Computer Methods in Applied Mechanics and Engineering*, 199(5):357–373, January 2010.
- [4] S. Morganti, F. Auricchio, D. J. Benson, F. I. Gambarin, S. Hartmann, T. J. R. Hughes, and A. Reali. Patient-specific isogeometric structural analysis of aortic valve closure. *Computer Methods in Applied Mechanics and Engineering*, 284:508–520, February 2015.
- [5] D. Schillinger, J. A. Evans, A. Reali, M. A. Scott, and T. J. R. Hughes. Isogeometric collocation: Cost comparison with Galerkin methods and extension to adaptive hierarchical NURBS discretizations. *Computer Methods in Applied Mechanics and Engineering*, 267:170–232, December 2013.
- [6] J. A. Cottrell, T. J. R. Hughes, and A. Reali. Studies of refinement and continuity in isogeometric structural analysis. *Computer Methods in Applied Mechanics and Engineering*, 196(41):4160–4183, September 2007.
- [7] T. J. R. Hughes, J. A. Evans, and A. Reali. Finite element and NURBS approximations of eigenvalue, boundary-value, and initial-value problems. *Computer Methods in Applied Mechanics and Engineering*, 272:290–320, April 2014.
- [8] T. J. R. Hughes, A. Reali, and G. Sangalli. Duality and unified analysis of discrete approximations in structural dynamics and wave propagation: Comparison of p-method finite elements with k-method NURBS. *Computer Methods in Applied Mechanics and Engineering*, 197(49):4104–4124, September 2008.
- [9] V. Puzyrev, Q. Deng, and V. Calo. Spectral approximation properties of isogeometric analysis with variable continuity. *Computer Methods in Applied Mechanics and Engineering*, 334:22–39, June 2018.

- [10] L. Brillouin. *Wave propagation in periodic structures;: Electric filters and crystal lattices*. Dover Publications, 2nd edition edition, January 1953.
- 525 [11] T. J. R. Hughes. *The Finite Element Method: Linear Static and Dynamic Finite Element Analysis*. Mineola, NY, 2003.
- [12] G. Strang and G. Fix. *An Analysis of the Finite Element Method*. Wellesley-Cambridge Press, Wellesley, Mass, 2nd edition edition, May 2008.
- [13] J. A. Cottrell, T. J. R. Hughes, and Y. Bazilevs. *Isogeometric Analysis: Toward Integration of CAD and FEA*. Chichester, West Sussex, U.K. ; Hoboken, NJ, August 2009.
- 530 [14] J. A. Cottrell, A. Reali, Y. Bazilevs, and T. J. R. Hughes. Isogeometric analysis of structural vibrations. *Computer Methods in Applied Mechanics and Engineering*, 195(41):5257–5296, August 2006.
- [15] R. R. Hiemstra, T. J. R. Hughes, C. Manni, H. Speleers, and D. Toshniwal. A Tchebycheffian Extension of Multi-degree B-Splines: Algorithmic Computation and Properties. *SIAM Journal on Numerical Analysis*, 58(2):1138–1163, January 2020. Publisher: Society for Industrial and Applied Mathematics.
- 535 [16] D. Toshniwal, H. Speleers, R. R. Hiemstra, C. Manni, and T. J. R. Hughes. Multi-degree B-splines: Algorithmic computation and properties. *Computer Aided Geometric Design*, 76:101792, January 2020.
- [17] Q. Deng and V. Calo. A boundary penalization technique to remove outliers from isogeometric analysis on tensor-product meshes. *arXiv:2010.08159 [cs, math]*, October 2020. arXiv: 2010.08159.
- 540 [18] S. S. Rao. *Mechanical Vibrations in SI Units*. Pearson, 6th edition edition, November 2017.
- [19] R. Szilard. *Theories and Applications of Plate Analysis: Classical, Numerical and Engineering Methods*. Wiley, Hoboken, NJ, January 2004.
- [20] C. de Boor. *A Practical Guide to Splines*: 27. New York, November 2001.
- [21] L. F. Leidinger, M. Breitenberger, A. M. Bauer, S. Hartmann, R. Wüchner, K. U. Bletzinger, F. Duddeck, and L. Song. Explicit dynamic isogeometric B-Rep analysis of penalty-coupled trimmed NURBS shells. *Computer Methods in Applied Mechanics and Engineering*, 351:891–927, July 2019.
- 545 [22] M. Breitenberger, A. Apostolatos, B. Philipp, R. Wüchner, and K. U. Bletzinger. Analysis in computer aided design: Nonlinear isogeometric B-Rep analysis of shell structures. *Computer Methods in Applied Mechanics and Engineering*, 284:401–457, February 2015.
- 550 [23] Y. Guo, J. Heller, T. J. R. Hughes, M. Ruess, and D. Schillinger. Variationally consistent isogeometric analysis of trimmed thin shells at finite deformations, based on the STEP exchange format. *Computer Methods in Applied Mechanics and Engineering*, 336:39–79, July 2018.
- [24] G. H. Golub and C. F. Van Loan. *Matrix Computations*. Johns Hopkins University Press, Baltimore, fourth edition edition, February 2013.
- 555 [25] Y. Saad. *Numerical Methods for Large Eigenvalue Problems*. Society for Industrial and Applied Mathematics, Philadelphia, revised edition edition, May 2011.
- [26] R. A. Horn and C. R. Johnson. *Topics in Matrix Analysis*. Cambridge University Press, Cambridge, 1991.